Department of Physics and Astronomy

University of Heidelberg

Diploma thesis

in Physics

submitted by

Marco Holzwarth

born in Sinsheim (Baden)

February 2010

Kinematically Complete Study on Positron Impact Ionisation of Helium

This diploma thesis has been carried out by Marco Holzwarth at the

Max-Planck-Institute for Nuclear Physics

under the supervision of

Priv.-Doz. Dr. Alexander Dorn

Two roads diverged in the wood and I, I took the one less traveled by, and that has made all the difference.

Robert Lee Frost

Zusammenfassung

Im Rahmen dieser Arbeit wurde die Einfachionisation von Helium durch Positronenstoß bei einer Projektilenergie von 80 eV experimentell untersucht. Hierzu wurde ein eigens modifiziertes Reaktionsmikroskop mit dem alle drei Endzustandsteilchen impulsaufgelöst nachgewiesen werden können an das Strahlrohr der Positronenquelle NEPOMUC am Forschungsreaktor FRMII in Garching angeschlossen. Um die Positronen mit möglichst geringem Verlust an Intensität vom starken Magnetfeld des Strahlrohrs in das schwächere Feld des Reaktionsmikroskops zu leiten, wurden Solenoidspulen, die einen adiabatischen Feldverlauf bewirken, im Übergangsbereich angebracht. Ein ausgefeiltes Verfahren zur Datenauswertung wurde entwickelt damit der zeitliche Ursprung des Ionisationsprozesses auch bei Verwendung eines kontinuierlichen Projektilstrahls gefunden werden kann. Schliesslich konnten dreifach koinzidente Ereignisse, welche aus der Fragmentation stammen, bestimmt werden. Für diese Ereignisse konnten wir die dreidimensionalen Impulsvektoren der drei Teilchen im Endzustand erhalten. Die erhaltenen Wirkungsquerschnitte zeigen, dass die im Vergleich zur Elektronenstoßionisation umgekehrte Projektilladung eine starke Emission des ionisierten Elektrons mit dem Projektil in Vorwärtsrichtung bewirkt.

Abstract

Within this work presented here, single ionisation of helium by impact of 80 eV positrons was studied in a kinematically complete experiment. Therefore, a dedicated reaction microscope was connected to the beamline of the NEPOMUC positron source located at the research reactor FRMII in Garching. Using a reaction microscope the momenta of all particles in the final state can be detected. In order to guide the positrons from the high magnetic field of the beamline into the lower field of the reaction microscope with a minimal loss on intensity, solenoidal coils producing an adiabatic field change have been installed at the transition region. A sophisticated method for the data analysis was developed to reconstruct the time origin of the ionisation process also for the case of a continuous beam. Finally, we were able to identify triple coincident events originating from the fragmentation. The three-dimensional momentum vectors of the three particles in the final state could be obtained for these events. The gained cross sections show that the projectile charge which is inverse compared to electron collisions causes a high emission of the ionised electron with the projectile in forward direction.

Contents

1 Introduction

The relationship between the energy E and momentum $\vec{p}$ of a free particle is given by Einstein's famous energy-momentum equation $E^2 = (cp)^2 + (mc^2)^2$ where m is the particle's mass and c denotes the vacuum speed of light. The solution of this equation for the case of an electron leads to an energy spectrum made up of two continuous bands separated by an interval $2mc^2$. The first of these correspond to negative energy states with $E = -\sqrt{(cp)^2 + (mc^2)^2}$ and the second to positive energy states with $E = \sqrt{(cp)^2 + (mc^2)^2}$. These results which seem quite unphysical at a first glance were interpreted by Dirac 1928 in his relativistic theory of electrons, which subsequently led to the prediction of the positively charged electron. Soon after Dirac's postulation, these positively charged electrons were observed by Anderson 1933 who also coined the term positron for these particles. The discovery of the positrons was also the first evidence of antimatter since the positron is the antiparticle of the electron having the same mass and spin as the electron and carrying the same amount of charge but with opposite sign. Although the positron is a stable particle under vacuum conditions, it will annihilate with an electron under the emission of radiation when it interacts with normal matter.

Low energy positron-atom collision studies contribute to the area of positron physics, which ranges from scientific basic research to technological applications. Fundamental use of positrons include the formation of neutral antihydrogen atoms used for testing of quantum electrodynamics (QED) or fundamental symmetries in nature (CPT theorem) (Amoretti et al. 2002 and Gabrielse et al. 2002). On the other hand, technological applications of positrons are numerous and increasing. They include, for example, positron emission tomography (R.L. Wahl 2002) to study metabolic processes or material research, such as insulators with low dielectric constants in chip production or material characterisation (Schultz and Lynn 1988). Furthermore, positrons offer new ways to study a wide range of other phenomena, including atomic clusters, nanoparticles and plasmas (Surko et al. 1986).

All these applications depend on the fundamental understanding of the interactions between positrons and matter and, therefore, the study of positron collisions with atoms, molecules and solids is of great interest. Also the comparisons with phenomena observed with other projectiles, such as the electron can lead to better insight of the interactions since collisions involving positrons are different from analogous electron experiments. Reasons are the absence of the exchange interaction characteristic for electrons, or the repulsive static interaction between the positron and the atom, in contrast to the attractive electron-atom interaction or

the added richness of the positronium formation channel. Extending the range of projectiles to include protons and antiprotons can provide information about effects on the collision processes of different masses and charge and, hence, offer a test of various theoretical approximations. These theoretical models are motivated by the fact that even a three-body system cannot be solved in an analytic way and, hence, they rely on approximations about the described process or the need of enormous computation efforts. Therefore, experiments have always been crucial in order to verify and guide the modelling for these calculations.

The study of scattering reactions involving atoms and molecules is a long-standing field in atomic physics. The first experiments have been made in the early 1910s when Rutherford investigated the structure of atoms by the collisions of collimated particles from radioactive decay onto a thin layer of gold and the detection of the scattered particles (Rutherford 1911). Starting from these pioneering studies, numerous scattering experiments followed for various combinations of projectiles and targets such as ion-atom, photon-atom, electron-atom etc. Electron scattering by gas atoms and molecules has been investigated since the pioneering work of Ramsauer 1922 and Townsend and Bailey 1922 in the early 20th in the last century. Further improvements in electron impact studies arose with the helium ionisation experiments performed by Ehrhardt et al. 1969 where the momentum vectors of all continuum particles were determined. However, these traditional measurements were restricted to a certain geometry where the electrons are detected in coincidence using energy and angle sensitive detectors in one specific plane. Since one free electron is present in the initial state and two free electrons are measured in the final state, these kind of experiment became known as (e,2e) experiments. Another milestone for atomic and molecular scattering physics was the invention of the cold target recoil ion momentum spectroscopy (COLTRIMS) (Mergel 1996) and the reaction microscope (Moshammer et al. 1996) where the use of projection techniques overcomes the previous limitations on the experimentally accessible phase space. Such an apparatus allows the coincidence detection of all particles in the final state over essentially the full solid angle. For example, using a reaction microscope access to three-dimensional fully differential data was opened while these kinematically complete studies deliver the most stringent test for theoretical treatment and provide an important contribution to reach the detailed understanding of dynamic processes.

For the electron's antiparticle, the positron, the first cross sections for collisions with an atom were then measured in the early 1970s by Costello et al. 1972. Thus, the development in the field of positron scattering has in many respect followed that of the electron case. However, positron-atom collision experiments have been different in the aspect that sources for positrons are not accessible in the same way as for electrons. Due to the nature of positrons, monoenergetic positron beams of high intensity are scarce. Therefore, existing experiments for positron impact ionisation suffer from the low positron beam currents obtained from radioisotope sources as

well as from low detection efficiencies of traditional electrostatic spectrometers. The points of contact between theory and experiment regarding positron scattering were greatly impeded by the lack of suitable low energy positron beam sources. Within the last decades, developments in high quality positron sources occurred and have made possible a host of experiments. For example, at the **NE**utron induced **PO**sitron source **MU**ni**C**h, NEPOMUC (Hugenschmidt et al. 2002), here, positron-electron pairs are produced by absorption of high energy γ-radiation released by the capture of thermal neutrons in cadmium. The neutrons are obtained from the research reactor FRMII located in Munich. The generated positrons are extracted and further moderated until they are guided in the beamline where the positrons can be used for various experiments. NEPOMUC claims to deliver the world's highest positron intensity of up to 10^9 low energetic positrons per second.

The intention of this work was the combination of both unique techniques, on one hand the reaction microscope with its capability to enable the kinematically complete investigation of an ionisation process and on the other hand the positron beam of the NEPOMUC facility with its high flux on low energetic positrons. This pilot experiment was designed to deliver the first comprehensive benchmark cross section for antiparticle impact ionisation of atomic systems. Therefore, a reaction microscope dedicated for electron collision ionisation studies (Dorn et al. 1999, Dürr et al. 2006) was adapted to the requirements for positron scattering. The impact energy during this work was chosen to be 80 eV whereas helium was used as target. Since the continuous positron beam used did not allow the standard time-of-flight measurement of the final state particles an important part of this work was the development of an analysis algorithm in order to reconstruct the reaction's time origin which is necessary to obtain the momenta of all ionisation fragments.

The present work is organised in the following manner: at the beginning, a brief introduction into positron impact ionisation and a discussion of the most important theoretical models is given. After that, the experimental set-up is presented where the working principle of the positron source and the used reaction microscope is considered. The following chapter deals with the method implemented in order to analyse the data obtained in the experiment. Finally, the outcome of the experiment will be discussed and in the end an outlook including improvements of the present experiment will be given.

2 Positron impact ionisation on atoms

In this chapter physical background information relevant for this work is presented. First, a general introduction into positron impact on atoms is given. The basic reactions and interactions are described through the comparison between positron- and electron-atom collisions and a review on the recent status in positron scattering is made. Furthermore, the theoretical treatment of collision processes are discussed briefly.

2.1 Introduction into positron-atom collisions

When a charged particle scatters with an atom or a molecule several processes can occur which are distinguished by the final state. When the projectile and the target are scattered without change in their internal structure, e.g. kinetic energy is conserved and the number of free particles remains constant, this is known as *elastic* scattering. Whereas processes are called *inelastic*, when the projectile and (or) target particle undergo a change of their internal quantum state during the collision resulting in an energy transfer and in a possible change in the particle number.

As already remarked within the introduction, the study of collisions of positrons with neutral or charged particles is of relevance in different fields of science and technology. The comparison between scattering of positrons and electrons by the same atoms and molecules can reveal interesting similarities and differences since the leptonic counterparts differ only by the sign of their charge and the attendant properties. Thus, these comparisons may help to stimulate a better understanding of electron (and positron) collision process.

2.1.1 Comparison: positron vs. electron scattering

When we look at the difference between electron impact studies and collisions using its antiparticle as projectile, the dominant interactions have to be taken into account (see table 2.1.1) where fundamental differences may be discerned. The mean *static* interaction between the undistorted atom and the projectile has opposite signs in the case of e^- and e^+ due to their opposite charge. Because of the repulsion between

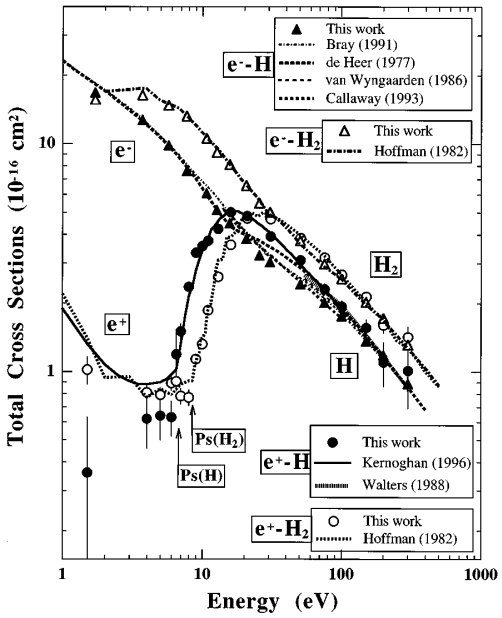

Figure 2.1: Comparison of $e^{\pm}$-H and $e^{\pm}$-H_2 scattering, from Zhou et al. 1997.

Interaction	e^-	e^+
Mean static	attractive	repulsive
Polarisation	attractive	attractive
Exchange	yes	none

Table 2.1: Dominant interactions contributing to $e^{\pm}$ scattering.

the positively charged lepton and the atomic nucleus, the static, short-range atomic potential is repulsive for positrons. Therefore, the positron does not penetrate far inside the atom. This kind of interaction contributes to $e^{\pm}$ scattering at all projectile energies. The *polarisation* interaction is, however, attractive for both e^- and e^+ and is relevant at sufficiently low incident projectile energies such that the target atom has an opportunity to polarise during the time of interaction. This leads to the long-range, attractive polarisation potential $V_{pol}(r) = -\alpha_d e^2/(2r^4)$, where α_d denotes the dipole polarisability of the atom. This asymptotic form is identical for electrons and positrons. At low positron energies, for which large separations play a important role, this polarisation potential can overcome the effects of the short-range repulsion, resulting in a net positron-atom attraction. Consequently, in the low energy regime, the opposite signs of the static and polarisation interactions in case of the positron give arise to a reduced scattering probability compared to electrons, as displayed in figure 2.1 for $e^{\pm}$-H scattering. The *exchange* interaction, which affects only electron scattering, originates from the antisymmetry of the total wavefunction of indistinguishable fermions since in the case of electron scattering two identical particles are detected in the final state. Therefore, this effect modifies electron scattering primarily in the energy region corresponding to the kinetic energy of the atomic electrons. At sufficiently high energies, the exchange and polarisation interactions will become more and more negligible, leaving only static interaction,

Scattering channel		Threshold energy
$e^{\pm} + A \rightarrow e^{\pm} + A$	elastic	none
$\rightarrow e^{\pm} + A^{*}$	electronic excitation	several eV
$\rightarrow e^{\pm} + A^{n+} + ne^{-}$	ionisation	several eV ($V_{ionisation}$)
$e^{+} + A \rightarrow A^{+} + \gamma's$	annihilation (e^{+} *only*)	none
$\rightarrow A^{+} + Ps$	positronium formation (e^{+} *only*)	$V_{ionisation} - 6.8$eV
$e^{\pm} + M \rightarrow e^{\pm} + M^{*}$	vibrational excitation	few $\times 0.1$eV
$e^{\pm} + M \rightarrow e^{\pm} + M^{*}$	rotational excitation	$< \times 0.1$eV

Table 2.2: Basic scattering channels open for positron and electron scattering by atoms and molecules. $V_{ionisation}$ refers to the threshold energy of ionisation. Adapted from Kauppila and Stein 1989.

which will result in a merging of corresponding $e^{\pm}$-atom scattering cross sections for the various scattering channels (refer to table 2.2) that are accessible for both projectiles.

The set of scattering channels that are possible only for positrons is richer, and therefore, much more interesting than those available under electron impact. The additional channels are annihilation and reactions based on positronium formation (both real and virtual). Positronium[1] (Ps) is the simplest bound state consisting of a single electron and a single positron and, thus, comparable to a hydrogen atom but with half the reduced mass and Bohr energy levels, $E^{n}_{\mathrm{Ps}} = -0.25/n^{2}$ a.u. For targets with ionisation potentials $V_{ionisation} < 6.8\,\mathrm{eV}$ - the ground-state binding energy of Ps - the positronium formation channel is open at all energies. Even for targets with $V_{ionisation} > 6.8\,\mathrm{eV}$ the Ps formation threshold is never far away. Hence, the positronium channel appears to have remarkable consequences and leads to stronger correlation effects in low-energy scattering compared to electron scattering.

2.1.2 Ionisation by positron impact

Using a reaction microscope, we are able to investigate the reaction channel for ionisation which is one of the most fundamental and basic collision processes. Especially, single ionisation of atomic hydrogen is one of the simplest dynamical few-body problems beyond the analytically solvable two-body problem where exactly three particles (one positron, one electron and the proton) are involved. In this work the ionisation of helium - the simplest correlated bound two-electron system - is studied

[1] So named by A.E. Ruark, see Ruark 1945.

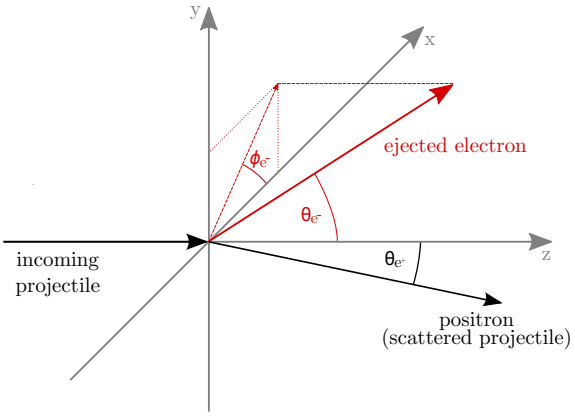

Figure 2.2: Geometry of the ionising collision.

by a positron impact energy of 80 eV. At this energy range, the main processes by which a helium atom can be ionised are annihilation, Ps formation and direct single ionisation as expressed, respectively, by following reactions:

$$e^+ + He \rightarrow He^+ + 2\gamma \tag{2.1}$$
$$e^+ + He \rightarrow He^+ + Ps \tag{2.2}$$
$$e^+ + He \rightarrow He^+ + e^+ + e^- \tag{2.3}$$

While positronium formation and annihilation also result in ionisation (equation 2.1-2.3) in the following the term ionisation will be reserved for the process given in equation 2.3 which is studied in this work and where three separate particles (e^+, e^- and He^+) result from fragmentation. The threshold of this reaction channel is $V_{ionisation} = 24.6\,\text{eV}$ for helium atoms, whilst annihilation[2] is always exothermic and Ps formation has a threshold energy given by $V_{\text{Ps}} = V_{ionisation} - 6.8\,\text{eV}/n^2$.

The results of scattering experiments are usually given in terms of quantities called *cross sections* σ and is defined, according to Bransden and Joachain 2003, as "transition probabilities per unit time, per unit target scatterer and per unit flux of the incident particles in respect to the target". With the target density n, the particle current in the projectile beam I and the length of the interaction volume l, the *total* cross section σ_{tot} of a scattering process which takes all possible reaction channels into account is linked to the count rate R of a measurement by

$$R_{tot} = \sigma_{tot} \cdot n \cdot I \cdot l. \tag{2.4}$$

In order to gain more information of a specific reaction's kinematic, the total cross

[2]Annihilation is not a significant effect expect at energies which are well below those ($> 0.2\,\text{eV}$) used in e^+-scattering experiments and its cross section is up to 10^{-5} smaller than for elastic scattering, see Massey 1976.

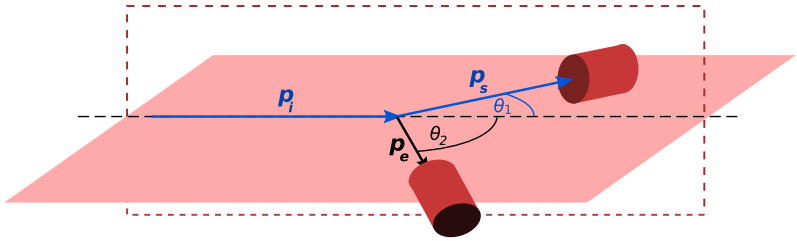

Figure 2.3: Conventional (e,2e) set up. The scattering plan is indicated in red (solid), with the projectile's momentum (p_i), the scattered projectile (p_s), the ejected electron (p_e) and their respective scattering angles. The perpendicular plane is shown in dashed red. Adapted from Pflüger 2008.

section is not sufficient. Therefore, the *differential* cross section is used which gives the probability distribution of different kinematic quantities. A kinematically complete determination of a three-body continuum final-state in an atomic scattering process, such as single ionisation like in our case, would require, in principle, the knowledge of nine variables. Here, the components of the momenta associated to each of the three particles in the final state have to be known. However, using momentum and energy conservation reduces the number to five. Regarding the solid angle intervals $\Delta\Omega$[3] for which a count rate is measured, we get a three fold differential cross section. In literature, this is often referred to as the *triply differential* cross section (TDCS) - which is defined by the solid angle for the scattered positron Ω_{e^+} and for the outgoing electron Ω_{e^-} and by the energy energy of the electron E_{e^-} (see figure 2.2). Thus, the complete kinematic for a reaction is determined by these three quantities and the differential cross section for positron impact single ionisation is given by $\partial^{(3)}\sigma/\partial E_{e^-}\partial\Omega_{e^+}\partial\Omega_{e^-}$. The specific event rate obtained in the measurement is then related with the triply differential cross section by

$$R(E_{e^-},\Omega_{e^+},\Omega_{e^-}) = \frac{\partial^{(3)}\sigma}{\partial E_{e^-}\partial\Omega_{e^+}\partial\Omega_{e^-}} \cdot n \cdot I \cdot l \cdot \Delta E_{e^-} \cdot \Delta\Omega_{e^+} \cdot \Delta\Omega_{e^-}, \tag{2.5}$$

where ΔE_{e^-} and $\Delta\Omega_{e^\pm}$ denotes the energy and the solid angle intervals for which the rate was obtained. In order to trace the determinants of a particular process, for example the importance of different mechanisms, fully differential data allow a deeper insight. Furthermore, these kinematically complete measurements enable a sensitive check of various approaches which deliver a theoretical model for the problem. In common scattering experiments, for example conventional (e,2e) experiments using two individual electron detectors for the detection of the scattered projectile and

[3]The solid angle Ω represents one independent variable consisting of the azimuth angle ϕ and the polar angle θ (see figure 2.2).

the ejected electron, the fully differential cross sections are determined directly by the specific coincidence count rate which is measured for a fixed set of energies and angles. The parameter space is then scanned sequentially by aligning the detectors to a new geometry (compare figure 2.3). Using a reaction microscope - more details are given in section 3.2 - we are able to detect the fragments of the ionisation over essentially the full solid angle and we are not restricted to a certain geometry.

The link between the experimentally obtained cross section and the theoretical quantum mechanical description is given by the relation:

$$\sigma \propto |T_{if}|^2, \tag{2.6}$$

where T_{if} is the quantum mechanical transition amplitude. The matrix element T_{if} represents the transition from the initial quantum state $|i\rangle$ to the final state $|f\rangle$ and is denoted by

$$T_{if} = \langle f | \hat{\epsilon} | i \rangle = \int \psi_f^* \hat{\epsilon} \psi_i \, \mathrm{dr} \tag{2.7}$$

where ψ_i and ψ_f are the wave functions in the initial and in the final state, respectively, and $\hat{\epsilon}$ stands for the operator containing the information about the transition process.

2.1.3 Cross sections

In this work, single ionisation of helium by positron impact with an energy of 80 eV is studied. In order to gain a better understanding of positron scattering processes, recent investigation in the area of positron collision research are reviewed in the following section. Therefore, cross sections, both for the whole scattering process and for individual reaction channels, are presented in a brief way, where, again, comparisons between electron and its antiparticle are made.

Total cross sections

The inert gases have been the first atoms which have been experimentally studied - for collisions with electrons as well as with positrons - as they available in atomic form as target gas at room temperature. Figure 2.4 gives an general comparison of measured total cross sections σ_{tot} for positrons and electrons scattering from He, Ne, Ar, Kr and Xe. The total scattering cross section can be partitioned into the sum of the integrated partial cross sections for each channel or process of interaction:

$$\sigma_{tot} = \sigma_{el} + \sigma_{ps} + \sigma_{ex} + \sigma_{ion} \tag{2.8}$$

where σ_{el}, σ_{ps}, σ_{ex} and σ_{ion} are the integrated partial cross sections for the elastic, positronium formation, excitation and ionisation channels, respectively. As already mentioned, in this work the term ionisation refers to a reaction according to equation

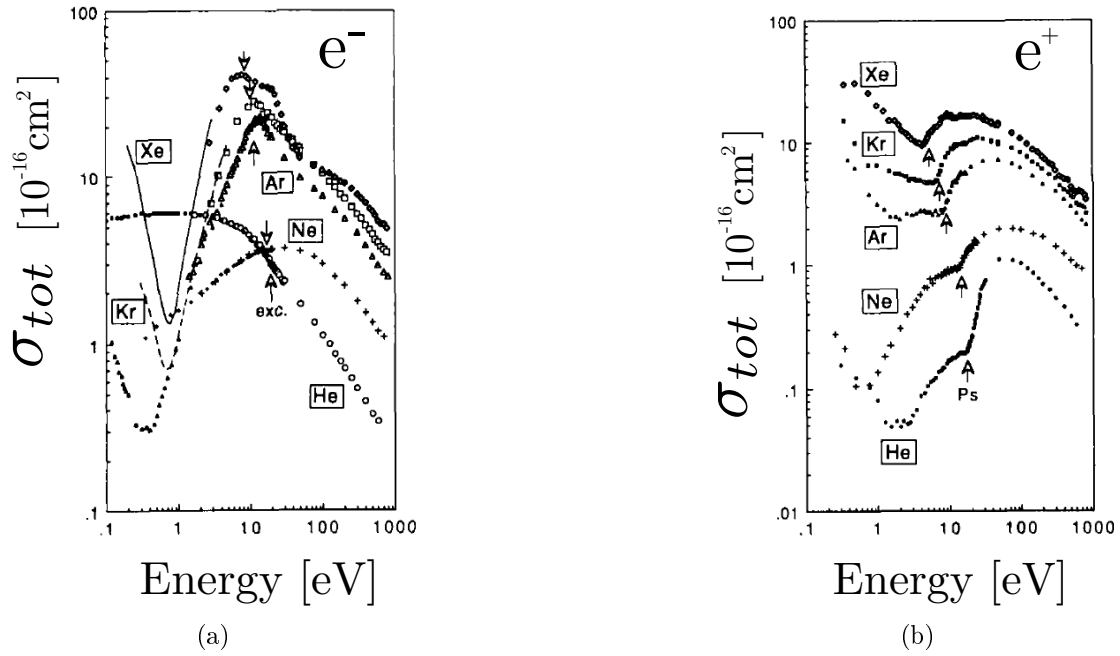

Figure 2.4: Total cross sections for noble gases. (a) Electron scattering. (b) Positron scattering. Adapted from Kauppila and Stein 1989.

2.3 where the ejected electron, the ion and the scattered positron are detected in the final state since reaction 2.2 also leads to ionisation of the target atom.

Regarding figure 2.4, below the lowest thresholds for inelastic scattering channels - electronic excitation for electrons and positronium formation for positrons - σ_{tot} represents only elastic scattering. One can observe in the case of e^--scattering that very deep minima occur at low energies (< 1 eV) for Ar, Kr and Xe. These minima are referred to as Ramsauer-Townsend effect[4] and arise from a net attractive interaction between the incoming projectile and the target atom. The Ramsauer-Townsend effect can be seen for He and Ne regarding e^+-scattering. Therefore, at low energies the polarisation interaction must be dominating the static interaction since a net attractive interaction is required. Furthermore, the σ_{tot} curves for e^+ suddenly increase as the projectile energy is increased through the Ps formation threshold. Hence, this feature suggests that the Ps formation channel plays an important role in positron scattering with the inert-gas atoms. For the total cross sections representing electron scattering, the maximum values occur at energies either near or below the lowest energy inelastic threshold, implying that e^--scattering at the energies of the maxima is dominated by elastic scattering.

[4]Named after Ramsauer and Townsend since they first observed the effect, see Ramsauer 1922 and Townsend and Bailey 1922

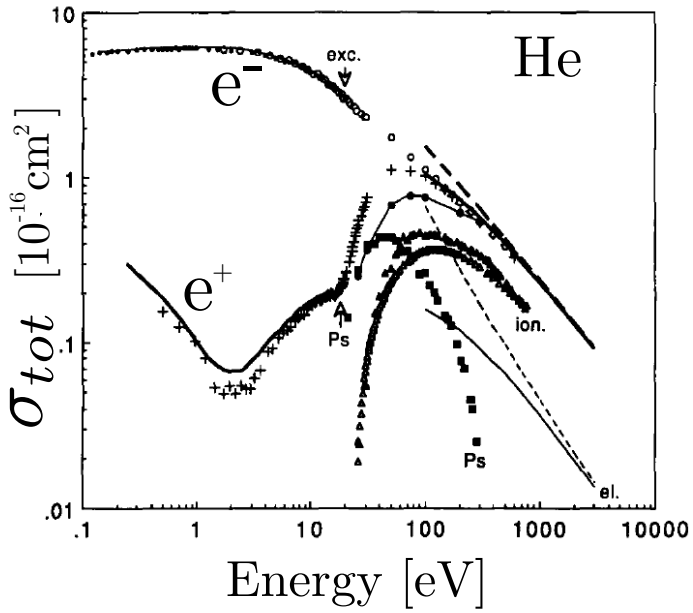

Figure 2.5: Total cross section for $e^{\pm}$-scattering with helium. Adapted from Kauppila and Stein 1989.

A more detailed view on the total cross section of positron an electrons collision with helium is presented in figure 2.5 as this system is the main topic of this work. Regarding the energy region of elastic scattering, the σ_{tot} for electron scattering is more than ten times larger than for positron scattering. This arises from the tendency for the static and the polarisation interaction to add for electrons and to cancel for positron. Coming to higher energies, the cross sections conform to each other and join for energies above 200 eV. Hence, charge sign effects are negligible as predicted by the first Born approximation (compare section 2.2.1) where the cross sections are independent from the sign of the charge and the collision is considered to be a single step two-body process.

Ionisation cross sections

The total ionisation cross sections, including all channels leading to an ion in the final state (see equations 2.1 - 2.3), for positron impact on helium is shown in figure 2.6(b). The integral cross section for direct ionisation on He, where only the reaction with three fragments in the final state is considered, is illustrated in figure 2.7(a) and the one for positron formation is given in figure 2.7(b). Experimental data for differential ionisation cross sections, in which the angular and/or energy distribution of the final-state particles are determined and, therefore, offer greater insights into the dynamics of the collision process, are relatively scarce for positron scattering.

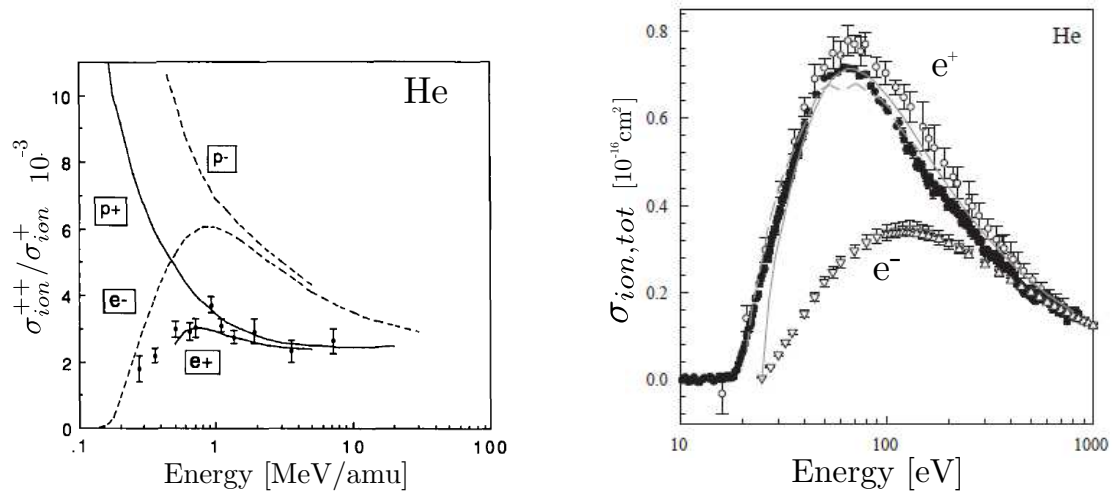

Figure 2.6: (a) Ratios of double σ_{ion}^{++} to single σ_{ion}^{+} ionisation cross section for positrons (e^+), electrons (e^-), protons (p^+) and antiprotons (p^-) scattering from He. The abscissa represents the projectile energy divided by the projectile mass (in atomic units), which is equal to the projectile velocity squared. Adapted from Kauppila and Stein 1989. (b) Total ionisation cross section for e^+-scattering on He. Taken from Laricchia et al. 2008.

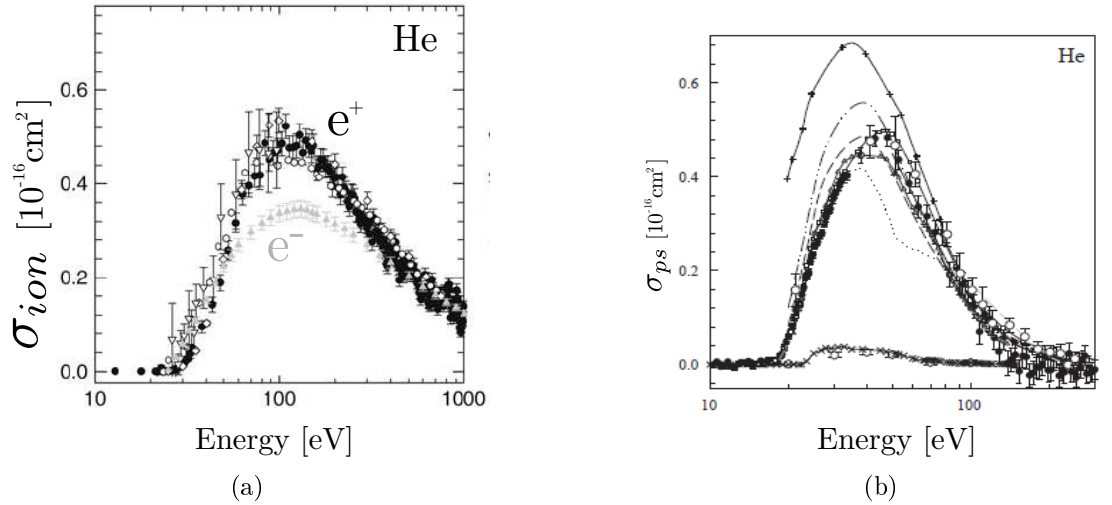

Figure 2.7: (a) Direct single ionisation cross section σ_{ion}^{+} in comparison with electron scattering. (b) Positronium formation cross section σ_{ps}. Both for positron collision on helium. Adapted from Laricchia et al. 2008.

Some quite interesting results have been founded by the analysis of the ratio of double to single ionisation cross sections ($\sigma^{++}_{ion}/\sigma^{+}_{ion}$) for helium when the ratios electrons and protons are compared with the ones of their counterparts, positrons and antiprotons. Comparative studies of atomic impact ionisation of particle/antiparticle pairs have been carried out in order to find differences resulting from the charge and the mass of the projectile[5]. The experimentally obtained ratios for these particles are presented in figure 2.6(a). For sufficiently high energies ($v^2 > 1\,\mathrm{MeV}/amu$), the ratios $\sigma^{++}_{ion}/\sigma^{+}_{ion}$ merge for each of the two projectiles having the same sign of charge even though their masses are notably different. The ratios for the leptonic particles ($e^{\pm}$) diverge and converge to zero at lower energies whereas they become very large for the baryonic particle/antiparticle pair. According to Charlton et al. 1988 this behaviour refers to the large differences in kinetic energy for the same velocity. At intermediate velocities, the single ionisation cross sections for the positively charged particles are higher than for their negatively charged counterparts due to polarisation attracting the ejected target electrons closer to the incoming positrons or protons. Since the cross section for single ionisation σ^{+}_{ion} slopes with increasing projectile energy as, for example, illustrated in figure 2.6(b), this implies that the energy dependency of the double ionisation cross section σ^{++}_{ion} behaves the same. Therefore, double ionisation mechanisms where the projectile interacts only once with the target contribute in the area for high velocities.

2.2 Theory: a brief overview

The simple ionization collision of a hydrogen atom by the impact of a structureless particle, the *three-body problem*, is one of the oldest unsolved problems in physics. The two-body problem was analysed by Johannes Kepler in the beginning of the 17th century and solved by Isaac Newton in end of the same century. However, the three-body problem is much more complicated and has no general analytic solution. Therefore, approximations or numerical methods have to be developed with the intention to get cross sections by calculating the quantum mechanical transition amplitude T_{if}. In order to handle the theoretical description of the ionisation process, simplifications have been assumed for the three-body kinematics in the final state, based on the fact that, for example, regarding a high energetic ion–atom collision, the fast projectile is marginal deflected, or in an electron–atom or positron–atom collision, one particle (the target nucleus) is much heavier than the two remaining.

In our case of inelastic atomic processes by scattering of a light, structureless particle, the available theoretical models can be divided into two groups, either a *perturbative* or a *non-perturbative* approach. In a perturbative method the scattering process is separated into an the initial and a final state whereas the interaction between the projectile and the target is is treated separately as a small perturbation,

[5]Compare, for example, with Schultz et al. 1991 or Knudsen et al. 1990

like in the Born approximation. This approach is mostly applied for experiments with high projectile energies but a perturbative model can hardly be applied for lower impact energies. Non-perturbative approaches, on the other hand, are dealing with a numerical solution of the Schrödinger equation which gives the quantum mechanical description of the system, for example the convergent close-coupling approach. Thus, they are convenient for scattering in the low energy range where the interaction between the projectile cannot be regarded as a marginal perturbation. These non-perturbative approaches have shown to deliver excellent agreement between theory and experimentally obtained data. Nevertheless, they require enormous computational effort. In the following, we will present some of the most important theoretical descriptions. Atomic units (see appendix A.3) are used for these consideration.

2.2.1 Born approximation

In order to solve a scattering problem like positron impact ionisation in a perturbative way[6], the system's Hamiltonian is separated into a unperturbed term $\hat{H}_0$ and the interaction potential $\hat{V}$. The unperturbed Hamiltonian $\hat{H}_0 = \hat{H}_{projectile} + \hat{H}_{target}$ splits further into the projectile and target system independent from each other prior and after the interaction. The Hamiltonian can be expressed like

$$\hat{H} = \hat{H}_0 + \hat{V} = \hat{H}_{projectile} + \hat{H}_{target} + \hat{V}. \tag{2.9}$$

Thus, the interaction potential $\hat{V}$ is regarded as a small perturbation to the otherwise free system. The eigenstates of the undisturbed system in the initial state can be written as

$$(\hat{H}_0 - E)\,|\Psi_{if}\rangle_0 = 0, \tag{2.10}$$

where $|\Psi_i\rangle_0$ and $|\Psi_f\rangle_0$ represent the product of respective free projectile - which can be written as a plane wave - and the target wave function $|\phi_{if}\rangle$ in the initial state and final state. The full or perturbed states $|\Psi_i\rangle$ and $|\Psi_f\rangle$ of the Hamiltonian $\hat{H}$ shall be given by

$$(\hat{H} - E)\,|\Psi_{if}\rangle = 0. \tag{2.11}$$

A possible, formal solution for this equation can be derived by the following expressing:

$$|\Psi_{if}\rangle = |\Psi_{if}\rangle_0 + \hat{G}_0^+ \hat{V}\,|\Psi_{if}\rangle\,, \tag{2.12}$$

[6] A more comprehensive introduction in scattering theory can be found in Bransden and Joachain 2003 or Sakurai 1993.

which is known as the Lippmann-Schwinger equation of potential scattering with the Green operator

$$\hat{G}_0^+ = \lim_{\epsilon \to 0} \frac{1}{E - \hat{H}_0 + i\epsilon}. \tag{2.13}$$

The Green operator describes the propagation of the system between individual interactions and is defined positive in order to guarantee that the scattered wave is outgoing. However, the function $|\Psi_{if}\rangle$ on the right hand side of equation 2.12 is still unknown. By iteratively inserting the Lippmann-Schwinger equation into itself, one obtains a series for the transition matrix element T_{if}:

$$T_{if} := \langle \Psi_f | \hat{V} | \Psi_i \rangle = \langle \Psi_f |_0 \hat{V} | \Psi_i \rangle_0 + \langle \Psi_f |_0 \hat{V} \hat{G}_0^+ \hat{V} | \Psi_i \rangle_0 + \ldots \tag{2.14}$$

This is called the *Born series* and it represents an expansion in powers of the interaction $\hat{V}$.

In the case of scattering a charged, structureless particle with a atom, the interaction term $\hat{V}$ is used to be the Coulomb potential between the projectile and target particles and, thus, can be expressed like

$$\hat{V} = -\frac{Z_P Z_T}{r_p} + \sum_{i=1}^{N} \frac{Z_P}{|\vec{r}_p - \vec{r}_i|} \tag{2.15}$$

where Z_P is projectile charge, $\vec{r}_p$ the projectile coordinate and $\vec{r}_i$ the distance between the nucleus and the target electrons.

The first Born approximation

When we just consider the first term of the Born series (equation 2.14), the transition matrix element in first Born approximation is the given by

$$T_{if}^1 := \langle \Psi_f |_0 \hat{V} | \Psi_i \rangle_0 . \tag{2.16}$$

Furthermore, the initial state is expressed by a product of a plane wave for the incoming projectile having momentum $\vec{k}_i$ and the eigenstates of the target (for example $|\Psi_i\rangle = \left|\vec{k}_i\right\rangle |\phi_i\rangle$). The outgoing projectile is also described by a plane wave which denotes that the interaction of the scattered projectile with the fragments is neglected. The transition amplitude for the first Born approximation is then given by

$$T_{if}^1 = \frac{Z_P}{2\pi^2 q^2} \langle \phi_f | \exp[i\vec{q} \cdot \vec{r}] | \phi_i \rangle , \tag{2.17}$$

with the momentum transfer $\vec{q} = \vec{k}_f - \vec{k}_i$. In order to calculate this first-Born-amplitude, only the the bound states $|\phi_i\rangle$ and the states in the continuum $|\phi_f\rangle$

of the undistorted target have to be determined which is exactly possible in the case of atomic hydrogen. However, for targets with more than one electron the deployment of the exact wave functions is quite complicated. Since the cross sections are proportional to the square of the transition amplitude (see equation 2.6), the cross sections are independent of the projectile's charge and, therefore, no difference should occur in the regime of high energetic collisions between electron and positron scattering.

The second Born approximation

In the matrix element for the second order Born approximation, in addition, the second order term has to be taken into account

$$T_{if}^2 = \langle \Psi_f |_0 \, \hat{V} \lim_{\epsilon \to 0} \frac{1}{E - \hat{H}_0 + i\epsilon} \, \hat{V} \, | \Psi_i \rangle_0 \,, \tag{2.18}$$

which considers scattering processes where the projectile interacts twice with the target. Thereby, a lot of possibilities exists, for example the projectile can scatter with nucleus and a bound electron. Additionally, the interaction of the projectile with the ejected electron after the collision (so called *post collision interaction*, PCI) are regarded, since an ionised electron is able to interact a second time with the projectile. Using the second-Born-amplitude, the agreement between theory and experiment can be improved. The cross section of the second Born approximation is then given by:

$$\sigma^{2ndB} \propto |T_{if}^1 + T_{if}^2|^2 = |\alpha_1 Z_P + \alpha_2 Z_P^2|^2 = \alpha_1^2 Z_P^2 + 2\alpha_1 \alpha_2 Z_P^3 + \alpha_2^2 Z_P^4, \tag{2.19}$$

$\alpha_{1,2}$ are coefficients which are determined by the explicit calculation of the transition amplitudes. In equation 2.19 the first term corresponds to pure one-step-process where the projectile interacts only once with the target, whereas the last term stands for a pure two-step-process considering exactly two interaction steps. The term in the middle represents an interference between these two pure processes which indicates a dependence of the cross section on the sign of the projectile's charge. Therefore, in the second order Born approximation appearance of charge effects for $e^{\pm}$-scattering should occur.

2.2.2 Distorted wave methods

An extension of the above described Born approximation is the approach using *distorted* waves where the interaction term $\hat{V}_{i,f}$ is separated in both the initial and final state:

$$\hat{V}_{i,f} = \hat{U}_{i,f} + \hat{W}_{i,f}. \tag{2.20}$$

This method is quite similarly structured as the Born approximation whereas the plane waves are merely replaced by the distorted waves. The first term of equation 2.20 $\hat{U}_{i,f}$ takes care of an exact treatment of the interaction, whereas the second term describes small perturbations, similar to the Born expansion. The Lippman-Schwinger equation (2.12) is solved including only the so-called *distortion* term $\hat{U}_{i,f}$ which leads to following solution:

$$|\chi_{i,f}\rangle = |\phi_{i,f}\rangle + \hat{G}\hat{U}_{i,f}\,|\chi_{i,f}\rangle\,, \tag{2.21}$$

where the eigenstates for the distortion interaction are obtained in the initial and final state. The amplitude for the transition, again in *post* and *prior* form, can then be written as

$$\begin{aligned} T_{if} &= \langle\chi_f|\,\hat{U}\,|\Psi_i\rangle & (2.22)\\ &= \langle\Psi_f|\,\hat{U}\,|\chi_i\rangle\,. & (2.23) \end{aligned}$$

Up to now, no approximations have been applied while the scattering amplitude provides the freedom to shift part of the interaction appearing in the operator $\hat{V}$ into the wave function. In first order, an approximation of the scattering wave leads to the distorted wave Born approximation where the initial state could be expanded by

$$|\Psi_i\rangle \approx |\chi_i\rangle\,. \tag{2.24}$$

Analogue to the Born series, the next higher order is given by

$$|\Psi_i\rangle \approx |\chi_i\rangle + \hat{G}\hat{U}_i\,|\chi_i\rangle\,. \tag{2.25}$$

Using the distorted wave method, it is possible to treat some part of the interaction exactly, and other in an perturbative way. For example, with the distorted wave approach, the interaction of the projectile with the nucleus can be treated in the initial and final channel.

2.2.3 Convergent close-coupling

An approach, where the time-independent Schrödinger equation of the collision system is solved numerical in a non-perturbative way, is the *convergent close-coupling* framework. The initial work was developed by Bray and Stelbovics 1992 in order to study the excitation of atomic hydrogen by electron impact. Then this method has been extended to various other scattering situations, for example ionisation of hydrogen and helium by electron impact (see Fursa and Bray 1995). These calculations using the convergent close-coupling approach show very good agreement with experimental data, notably in the case of electron impact ionisation of helium (compare Stelbovics et al. 2005 and Dürr et al. 2006).

Furthermore, collision processes with positrons as projectiles can be studied using the convergent close-coupling approach, as for example positron hydrogen scattering (see Bray and Stelbovics 1993). Calculations with the convergent close-coupling method for positron scattering with helium - which is of special interest for this work - haven been done in Wu et al. 2004. The convergent close coupling calculations for electron collision process can be readily applied to the case of positron scattering by simply omitting the exchange term and changing the sign of the projectile's charge. In the close-coupling treatment, an expansion of the target system in a basis-set of eigenstates of the unperturbed target Hamiltonian is performed. This is constructed by the expansion in orthogonal so-called Laguerre functions whereas, due to practical reasons, only a finite number N of states are included in the calculation, hence the name close-coupling. Beside the "true" bound states in the target, also the continuum has to be taken into account which is approximated by so-called "pseudo"-states. The close-coupling method converges definitely for large N but an enormous computational effort is required to solve the numerical problem. This approach is also restricted to pure three-body problems which can be circumvented, for example in the case of helium, with the approximation of a *frozen core* where only the active electron is treated individually.

While the convergent close-coupling method uses a momentum space representation of the wavefunctions, a similar approach, the *exterior complex scaling* (ECS) developed by Rescigno et al. 1999, uses position space wavefunctions. The exterior complex scaling method was first applied to electron-atom ionization problems and was demonstrated to provide highly accurate ab initio solutions for electron-hydrogen collisions through direct solution of the time-independent Schrödinger equation in coordinate space. Recently, the framework of the ECS was extended to scattering processes with positrons as projectile (see Bartlett et al. 2007).

3 Experimental set-up

This chapter deals with details of the experimental set-up and techniques applied to gain information about single ionisation of helium by positron impact. First, a brief overview about the current status in positron beam development is given, followed by background information about the NEutron induced POsitron source MUniCh (NEPOMUC) where the experiment, discussed in this work, was performed (section 3.1). During the 20 day beam time in spring 2009 a reaction microscope[1] was connected to the beam line of NEPOMUC (see Hugenschmidt et al. 2002) which delivers a continuous beam of positrons. This reaction microscope[2] was originally dedicated for the study of electron impact ionising processes, and within the present work, was can be adapted also for positron projectiles.

Briefly, the beam from the positron source is crossed with a cold supersonic atomic target jet (section 3.2.1). The scattered projectiles as well as the target fragments are extracted by the spectrometer (section 3.2.2) and imaged onto two position and time resolving detectors (section 3.2.3). The particles' momentum vectors can be derived through its positions and times of flight. While the time measurement normally requires a pulsed projectile beam, the complete kinematics also can be obtained for continuous beams. This is realised by using redundant information from the detected triple coincidence of all continuum particles in combination with momentum and energy conservation. In order to direct positrons out of the strong magnetic guiding field of 60 Gauss of the beam line into the reaction microscope (6 Gauss) in a controlled way, a magnetic field transition section of a Zeeman slower-like coil tube is implemented (section 3.2.4).

3.1 The positron source

In the last decades great efforts have been made to develop positron beams of high intensity. Hence, various techniques have been applied based mainly on two principles for positron production: On the one hand positrons gained through β^+-decay of radioactive isotopes and on the other hand positron generation by pair production from absorption of γ-radiation.

Beams of the first category are realized in labs based on commonly available β-

[1] Initially described in Moshammer et al. 1996.

[2] The used reaction microscope is widely discussed in Dürr 2006

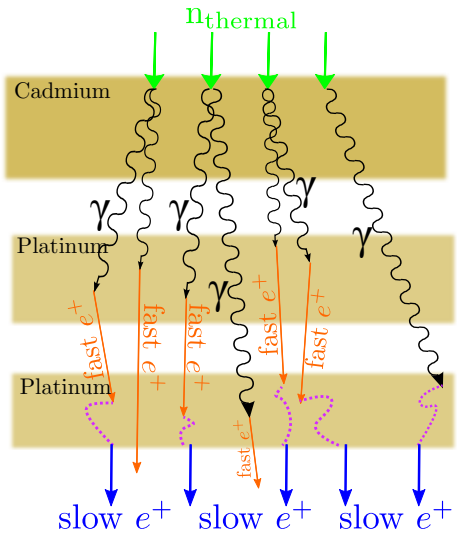

Figure 3.1: Working principle of the NEPOMUC source:
High energy γ-radiation is released through capture of thermal neutrons in Cd. The absorption of the prompt high energy gammas in Pt generates positrons by pair production. The fast electrons and positrons are further moderated in Pt. The deceleration process is indicated by dashed lines. Due to clarity, electrons also emerged through pair production are omitted.

sources like ^{22}Na or ^{58}Co. These conventional laboratory beam facilities[3] based on one of theses β^+ active isotopes and a positron moderator, mostly made of tungsten, are limited in intensity due to self-absorption of positrons in the source material. For this kind of sources, the yield of moderated positrons usually ranges between 10^4 and 10^6 positrons per second. Another way consists of dedicated materials which transform into short lived positron emitting isotopes upon exposure to thermal neutrons. For instance, sources based on the reaction $^{63}\mathrm{Cu}(n,\gamma)^{64}\mathrm{Cu}$ can yield continuous positron beams of about $10^7 \mathrm{e}^+$ per second after moderation.

The facilities summarised in the second group provide positrons generated through pair production from high energy γ-rays. Positrons can be obtained in a target or a beam dump of linear accelerators, where bremsstrahlung produces $\mathrm{e}^+\mathrm{e}^-$-pairs in the field of target nuclei. At a LINAC the flux of a slow positron beam can reach typically up to $5 \times 10^8\,\mathrm{e}^+$ per second (e.g. Suzuki et al. 1997). High energy γ-radiation is also available at reactors as primary γ-rays from nuclear fission or secondary γ-rays due to (n,γ)-reactions.

At the NEPOMUC facility - located in the Forschungsreaktor München II (FRM II, research reactor Munich II) - positrons are generated through pair production process as a result of thermal neutron capture in cadmium. The capture mechanism is totally dominated by the nuclear reaction $^{113}\mathrm{Cd}(n,\gamma)^{114}\mathrm{Cd}$ due to the enormous likelihood of this process. Its cross section amounts to 26,000 barn while ^{113}Cd has an abundance of 12.2% in natural cadmium. The resulting neutron binding energy of 9.05 MeV radiates, where on an average 2.3 photons with more than 1.5 MeV per captured neutron are released. The high energy of the γ-radiation is absorbed in a converter material to generate positrons by pair production. Platinum with its

[3] Köver et al. 1993 and Gilbert et al. 1997 research into beam facilities of this type. A more general overview concerning positron beams and their application can be found in Coleman 2000

high nuclear charge ($Z = 78$) is used as absorber substance since the cross section for pair production is roughly proportional to Z^2 and, therefore, materials with high nuclear charge Z are preferable. The emitted positrons show a broad energy distribution with the maximum located at a positron energy of 800 keV. To gain the required mono energetic positron beam the positrons pass a platinum moderator. Beside its high atomic number, the moderation property of platinum exhibits long-term stability under reactor conditions and its operation is much easier than the commonly used tungsten moderators. Positrons thermalised close to the surface can diffuse to the surface and are re-emitted with a certain probability.

The moderated positrons released into the vacuum receive the kinetic energy defined by the negative positron work function of $-1.8\,\mathrm{eV}$ in polycrystalline Pt. The positrons are extracted and accelerated by electric lenses and then guided magnetically out of the reactor core through a longitudinal field (6 – 7.5 Gauss) produced by a solenoid coil mounted on the beam tube. Transversal components of the earth magnetic field and the stray fields in the reactor shielding are compensated by correction coils arranged in pairs perpendicular to the beam axis. The latter are furthermore used to adjust the positron beam and so to minimise transport losses. In order to improve the beam's brightness a positron re-moderation stage is installed outside the reactor shielding. The main part of the re-moderator consists of a tungsten single crystal (1 1 0) in back reflection geometry. Finally, the e^+- beam passes a magnetic beam switch to distribute the positrons to the permanent installed experiments or the open beam port where temporary experiments can be connected to the beam line.

During our beam time in May 2009, FRM-II was operated at the nominal reactor power of 20 MW. NEPOMUC, the positron beam facility at FRM-II, claims to be the positron source to deliver the world's highest intensity of low-energy positrons, which is close to 10^9 moderated positrons per second Hugenschmidt et al. 2008. After re-moderation the positrons arrive with a current of $3\text{–}5 \times 10^7\,\mathrm{e^+/s}$ and an energy of 20 eV with a resolution of $\sim 1\,\mathrm{eV}$ (according to Piochacz et al. 2008) at the entrance of the reaction microscope. In there, the positrons are further accelerated while traversing the spectrometer up to an impact energy of 80 eV in the collision volume.

3.2 The reaction microscope

Beside the positron source, the other essential part of the experiment is a reaction microscope which is connected to the positron beam line. Following, the basic components forming the apparatus to measure fully differential cross sections (FDCS) are described. In our laboratory frame the z-axis is defined by the direction of the projectile beam which also corresponds to the spectrometer axis. The detectors span the (x, y)-plane and the $-y$ direction is given by the propagation direction of the gas jet.

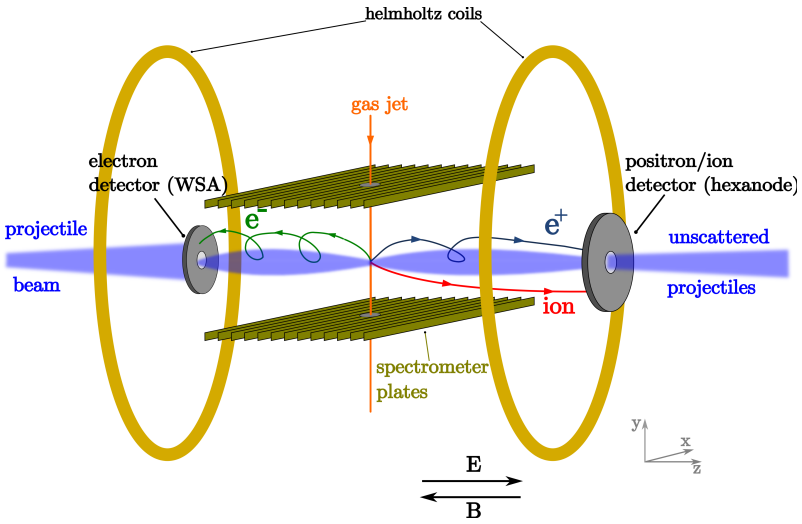

Figure 3.2: View of reaction microscope.

3.2.1 Target

Analysing atomic reactions requires all involved particles to be in a well-defined initial state. In particular the residual ion emerged from the ionising collision gains less than a few atomic units through the collision, which is much lower than its thermal momentum spread at 300 K. Therefore, the target atoms have to be cooled far below room temperature in order to achieve acceptable resolution. Applying adiabatic expansion to the atomic gas, temperatures in the magnitude of a few Kelvin can be reached. This corresponds to a very narrow energy distribution which is indispensable for high resolution momentum spectroscopy. Beside the internal cooling, also a high particle density can be realised in an atomic beam formed by the supersonic jet expansion.

The process of adiabatic expansion is technically implemented by letting gas with an initial temperature of T_i and pressure p_i spread through a tiny nozzle with diameter d into a chamber with much lower pressure p_b. Passing the nozzle, the atoms are accelerated resulting in a velocity of the jet higher than the local speed of sound for the reservoir with lower pressure.This area is called *zone of silence*. Through the adiabatic behaviour the systems entropy remains constant and therefore temperature decreases. In order to prevent the supersonic flow to break down, a small slit, the so called skimmer, is installed to form an atomic beam. Furthermore the internal momentum extension in transversal direction can be reduced by collimating the beam using a second skimmer, peeling off atoms with large velocity components in the plane perpendicular to the jet. In total, the gas jet has to pass three differentially pumped stages before reaching the main chamber volume, where the vacuum

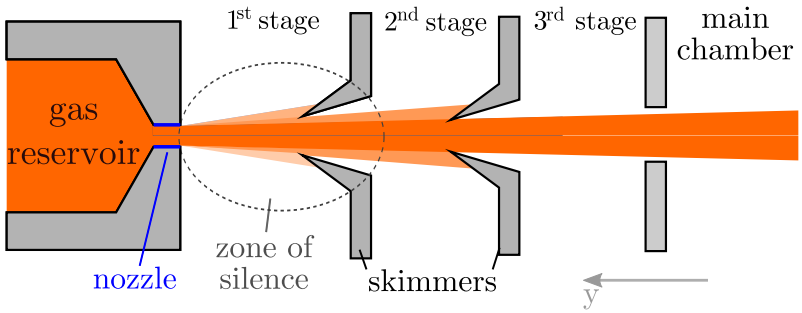

Figure 3.3: Formation of a supersonic gas jet by supersonic expansion through a tiny nozzle and elimination of high transversal momentum by two skimmers. Three differential pumping stages segregate the reaction volume from the high pressure gas reservoir, based on Senftleben 2009.

now is hardly influenced by particles of the gas jet. Additionally, a beam dump is installed at the bottom of the main chamber which further evacuates the unbroken atoms of the beam. In the experimental chamber the atomic beam formed by the gas jet is then crossed with the projectile beam. More details about the technical design and features of the jet system used are described in Höhr 2004, p 37.

The special characteristics of our supersonic jet especially the temperature in longitudinal direction can be obtained from gas dynamics, but here we will only present the main results already introduced in Miller 1988. Further aspects and theory of supersonic gas jets in particular concerning reaction-microscope can be found in Langbrandtner 2007. Using the formulae given by Miller 1988 the final temperature $T_{f\parallel}$ in expansion direction of the jet can be expressed by:

$$T_{f\parallel} = T_i \frac{\gamma}{\gamma - 1} \frac{1}{{S_\infty}^2}, \tag{3.1}$$

where S_∞ denotes the *terminal speed-ratio* between the propagation speed of the jet and the particles' thermal velocity within the jet. Furthermore, γ stands for the heat capacity ratio, which is constant for ideal gases and is defined by $\gamma = {}^{(d_f+2)}/_{d_f}$, where d_f is the number of active degrees of freedom. Helium used as target gas during the measurement at NEPOMUC has a heat capacity ratio of $\gamma = {}^5/_3$ as there are three active degrees of freedom (d_f=3) for mono atomic gases. Another advantage of helium is its small binding energy (1.1×10^{-7} eV) which prevents the gas to condensate in a reservoir of high pressure. Thus, operating the gas with a high initial pressure p_i results in a larger speed-ratio which is worthwhile to reach low temperatures in the jet. With the parameters for the present experiment were $p_i = 15$ bar for the initial pressure and $d = 30\mu$m for the nozzle's size, a speed-ratio of $S_\infty \approx 30$ can be determined from figure 2.11 in Miller 1988. $T_{f\parallel} = 0.8$ K is calcu-

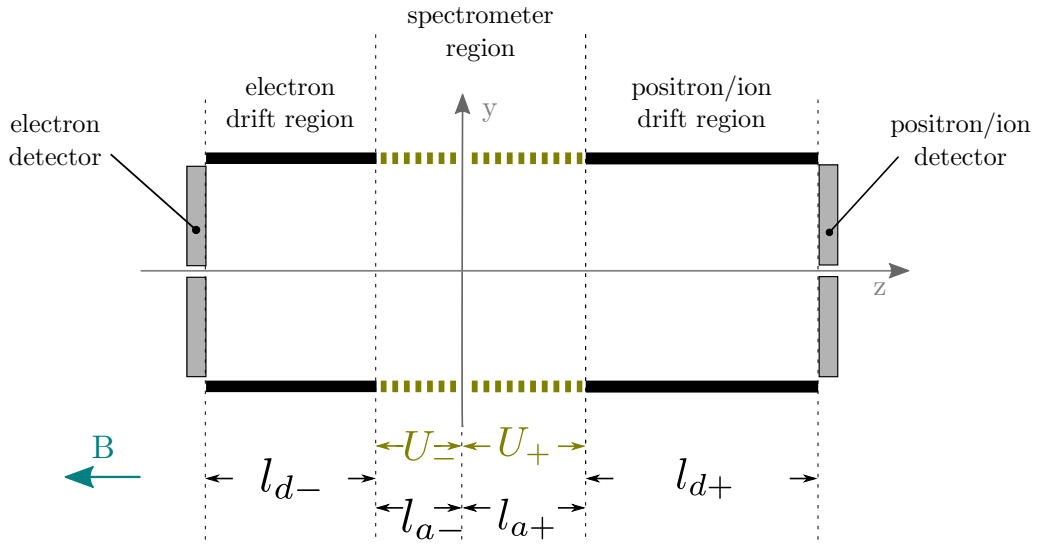

Figure 3.4: Schematic view of the reaction microscope dedicated for positron impact experiments at low impact energies.

lated for the given configuration using equation (3.1). This achievable temperature corresponds to a momentum distribution width of 0.32 a.u. Passing two skimmers the beam has also been collimated in the plane perpendicular to the jet direction resulting in a beam diameter of about 2 mm (FWHM) at the interaction point. In z-direction the influence of the target's position spread onto the time-of-flight of the charged fragments is negligible because of the *time-focussing*[4] configuration for the deployed spectrometer. According to Ferger 2006 where a similar set-up (same diameter of the nozzle, also helium as target gas, but a reservoir pressure p_i of 10 bar) was applied, the density of the jet at the interaction point can be estimated to the value of $1 \times 10^{12}\,\mathrm{cm}^{-3}$.

Supersonic jet expansion can also be applied to molecular gases where, additionally, the internal degrees of freedom - rotation and vibration - can be cooled.

3.2.2 Spectrometer

A benefit of a reaction microscope which is depicted in figure 3.2 is that not only all charged particles involved in the ionisation process are detected at once but that it covers the whole solid angle of 4π. This is achieved by applying homogeneous electric and magnetic fields which guide the fragments onto position sensitive detectors. The two-dimensional information (x, y) gained by the position detection is complemented through measurement of the particles' time-of-flight starting at the origin of the

[4] Closer consideration of time focussing concerning our reaction microscope has been done in Pflüger 2008

collision until the hit on the detector. In this way, one obtains all necessary data to reconstruct the complete three-dimensional momentum components for all fragments (compare section 4.3 for a detailed description of momentum calculation). In order to observe particles with different sign of charge two detectors are required. For this reason an electric field is applied which extracts negatively and positively charged pieces onto opposite directions.

In our work positrons and ions are accelerated on the detector for positively charged particles - henceforth it is called *positron/ion detector* - and the only fragments with negative charge namely the electrons are guided to the so-called *electron detector*. For the combined imaging of positron, ion and electron an additional homogeneous magnetic field is used. This restricts particles normally missing the detector due to their high transversal momentum back to the area covered by the detector. However, the influence of the B-field on the ions' trajectory is negligible because the mass of the ions is four orders of magnitude larger than for the lighter leptons taking part in the scattering process. The electric field which separates opposite charge was in the order of 180 $^{\mathrm{V}}/_{\mathrm{m}}$ during beam time at FRM-II while the magnetic field was adjusted to B $\approx$ 6 Gauss.

Directly after collision, the products of the fragmentation are accelerated within the spectrometer where the positrons and the ions are led in $+z$ direction over a length of $l_{a+} = 110\,\mathrm{mm}$ and then pass a field-free space called *drift* region with a length of $l_{d+} = 220\,\mathrm{mm}$. In $-z$ direction, thus on the extraction path for electrons, the length of the applied electric field area is $l_{a-} = 82\,\mathrm{mm}$ and the drift length is $l_{d-} = 164\,\mathrm{mm}$. The ratio between drift and acceleration length is determined to be $^{l_{dx}}/_{l_{ax}} = 2$ in order to fulfil the condition for the *time focussing*. The consequence of this effect is that the time of flight depends only on the initial momentum in longitudinal direction and is in first order independent on the z-position where the fragmentation occurs. In conclusion, the finite extension of the interaction volume becomes marginal and hence, there is no need of reducing the diameter of the target beam along the spectrometer axis. In this way one benefits of a larger interaction volume and finally a larger number of target atoms without loss of resolution. Larger overlap between positron beam and target jet is namely always favourable due to typically low cross sections for ionisation reactions. A more detailed discussion of time focussing regarding our reaction microscope was given in the appendix of Pflüger 2008.

The main challenge in combining a reaction microscope with electron or positron beams is the influence of the spectrometer's electric field and the applied magnetic field onto the primary projectile beam. Since the beam of positrons is coming along the spectrometer axis, the fields and the geometry of the spectrometer - the drift length and acceleration length in both directions - have to be adjusted in a way that the initial projectile beam passes the hole in the electron detector. Furthermore, the projectiles perform a helical trajectory in the magnetic field (compare figure 4.3) and so, one has to assure that the initial projectile beam is forced back onto the

spectrometer axis exactly in the reaction volume where the target jet crosses the z-axis. In addition, unscattered projectiles should not hit the detector in order to prevent the detector from saturation. Therefore, these unscattered positrons have to pass the hole in the MCPs of the hexanode detector which is achieved when they do again exact one cyclotron revolution on their way from the point of reaction to the detector. This situation is illustrated in figure 3.2. Some calculated values for the field and the geometry which fulfil these conditions are given in appendix A.1.

3.2.3 Position sensitive detectors

Beside its time-of-flight, it is necessary to know where a particle has hit the detector in order to gain all informations for the reconstruction[5] of its momentum vector. Therefore, the experiment was equipped with two position sensitive microchannel plate detectors. On the spectrometer side where the positrons and the recoil ions are detected, a multi-hit capable *hexagonal delay-line anode* (hexanode) Lampton et al. 1987 is used to resolve the fragments' position. For the electrons, a new *wedge-and-strip anode* (WSA) is applied which has a central hole for the passage of the projectile beam and allows good position resolution without need of sophisticated electronics Martin et al. 1981. A hole at the position of the spectrometer axis is implemented in both detectors. Furthermore, *microchannel plates*[6] (MCPs) are mounted before the position sensitive detectors. Thus, an amplification of the incident particles signal is achieved.

Microchannel plate

A MCP consists of an array of parallel orientated, micro fabricated channels (each with a diameter size $\approx 25\mu$m). These channels work as secondary electron amplifiers in the way that the initial incoming particle hits the wall of a channel and knocks out electrons. These secondary electrons are further accelerated in the channel by an applied potential difference between the front and the back (typ. 1 kV) of the MCP. As a result of the following cascade, a charge cloud at the exit of the channel is produced (see figure 3.5). This charge cloud hits the position encoding device (anode) which now allows to determinate where the reaction's fragment arrived on the MCP. The spatial resolution is only limited by the diameter of the channels and their spacing.

The front and back side of a MCP are coted with a metal substrate of low resistance and the individual channels are made of leaded glass. The amplification factor of a MCP ranges between 10^4 and 10^6, but can be enhanced by stacking together two MCPs. Further improvement for the yield of secondary electrons is reached by tilting the channels of an individual MCP and stacking both MCPs in a way

[5] See section 4.3 for a detailed discussion of the data reconstruct process.
[6] Review on MCPs are given in Wiza 1979.

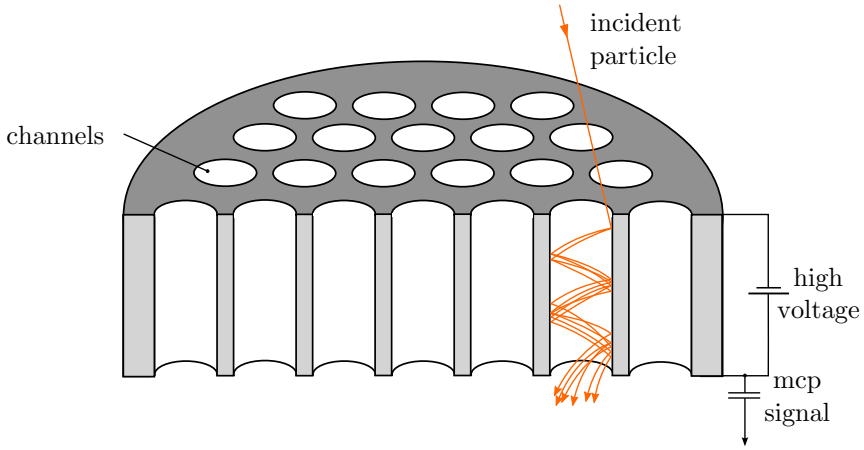

Figure 3.5: Working principle of microchannel plate, from Pflüger 2008

that a MCP channel form a slight angle with respect to the channel of the other MCP, a so-called chevron stack. Through this configuration the secondary electrons are forced to hit the channel's wall more often resulting in an improvement of the amount of charge. Additionally, this arrangement suppresses the escape of feedback ions which are created by ionising processes in residual gas or through escape from the channel walls. The impact of a particle on the MCP leads to a drop in the MCP voltage which is coupled out via a capacitor. This signal is used to derive the particle's time-of-flight with a typical time resolution of less than 1 ns.

Delay-line anode

In order to derive sufficiently resolved position information for positrons and ions, a *delay-line anode* is deployed at the end of the spectrometer. In a simple picture, a delay-line anode can be described as a wire wrapped around a thin insulating material as visualized in figure 3.6(a). The position is determined by measuring the time which the charge - induced by the electron avalanche from the MCP - needs to propagate to both ends of the wire. This is feasible since parts of the charge disperse in both directions of the wire. The time difference between the arrival signal at each end is proportional to the position coordinate at which the charge cloud is deposited. The current position in x-direction which is perpendicular to the direction of the wire is then given by:

$$x = \frac{v_\perp}{2} \cdot (t_1 - t_2) \tag{3.2}$$

where $v_\perp$ denotes the effective propagation speed of the pulse in direction of x. However, for our analysis procedure it is not required to know the exact value for $v_\perp$ as it is obtained indirectly by normalising the extend of coordinates to the real size of our detector. Performance improvements and reduction of noise can be achieved

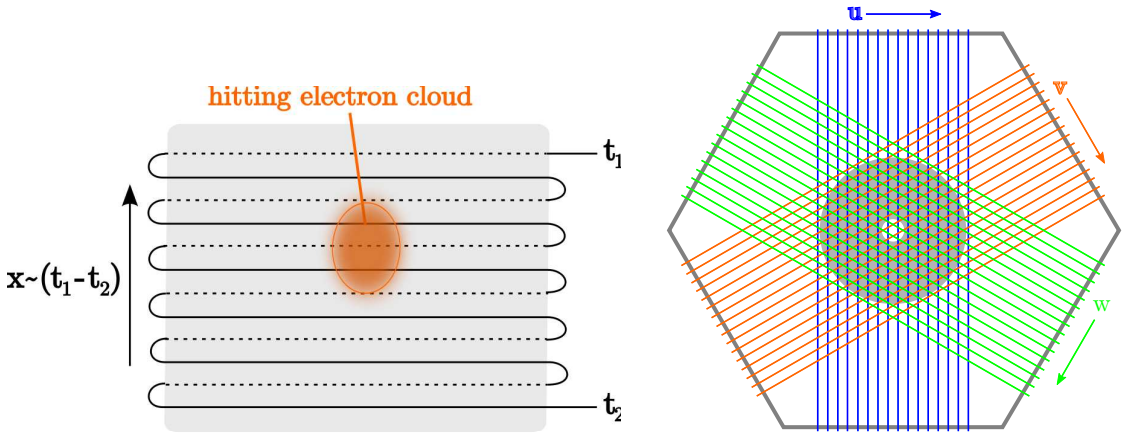

Figure 3.6: (a) Functionality of a delay-line anode layer, (b) design of the hexagonal anode used for positron/ion detection. Areas covered by the MCPs - forming the active detection region - are indicated in grey, from Senftleben 2009.

by the use of a second wire for each direction. Thereby, one presents a *reference*-wire while the *signal*-wire delivers the mark. By taking the signal difference using a differential amplifier, noise which is induced in both wires vanishes. The position resolution δx is mostly limited by timing electronics, but it is possible to reach an uncertainty of less than $\delta x = 0.5\,\mathrm{mm}$.

For two-dimensional information, at least two layers with an angle of 90° in respect of each other are necessary. The delay-line anode detector used in the present experiment at NEPOMUC is equipped with a third layer where the angles between the layer are now 60° (refer to figure 3.6(b)). Because of the hexagonal shape the design is also known as *hexanode*. The main purpose for the implementation of a third layer was to increase its multi-hit capability. The detector was originally dedicated for (e,2e)-experiments where it was quite substantial to detect two particles impinging onto the detector within a time frame in the nanosecond regime. Design and detailed study concerning time resolution for the used hexanode can be found in Haag 2006 and Dürr 2006. However, in the positron scattering experiment multi-hit capability is not that crucial. Beside the scattered positrons only ions with a longer time of flight ($> 14\,\mu\mathrm{ms}$) hit the detector. In addition, the microchannel plates in front of the hexanode have a central hole. The purpose of this hole is that the unscattered projectiles can pass through without saturating it. They do, however, not induce a position signal, since the number of positrons in the beam is less than the number of electrons in a charge cloud produced by the MCP. The method of reconstructing the particles' positions from the signal gained through the hexanode is described in more detail in section 4.2.

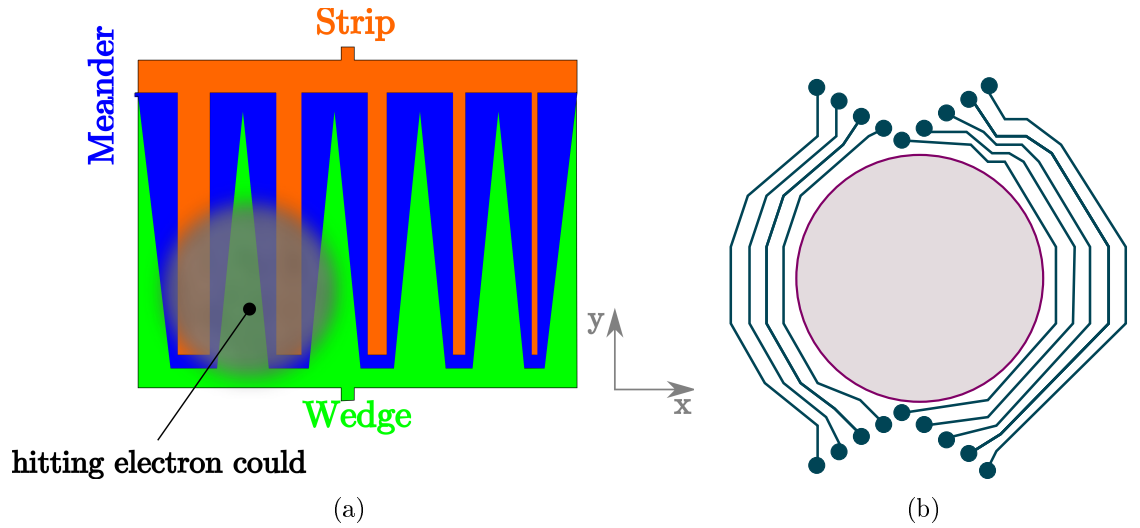

Figure 3.7: (a) Working principle of a wedge-and-strip anode. (b) Connectivity of the electrodes around the hole in the anode.

Wedge-and-strip anode

On the opposite side of the spectrometer a so called *wedge-and-strip anode* (WSA) is mounted for position detection of electrons emerged from the ionising fragmentation. In contrast to the hexanode where two particle per reaction have to be detected, multi-hit capability is not required for negatively charged particles. On the other hand, one benefits from a easier handling of the read out electronics as no sophisticated system - composed of differential amplifiers and discriminators - like for the hexanode, is needed. Furthermore, this anode type allows for a central hole for the passage of the primary beam which is a necessary feature in this experiment. The implementation of the hole is easier to handle for a wedge-and-strip anode and additionally, the resolution, especially in the central region around the hole, is improved compared to a hexanode. The three areas *wedge*, *strip* and *meander* - hence the name for the detector - with its specific structure (see figure 3.7) form individual electrodes. In order to reach a sufficiently large charge cloud, MCPs in chevron configuration are placed in front of the WAS. The electron avalanche generated in the MCP places different amount of charge on the electrodes. The fraction of charge depends on the position where it is deposited on electrodes. Hence, the centre of gravity of the cloud can be reconstructed through the knowledge of geometrical shape of these electrodes. As it is shown in figure 3.7, the zone covered by the *wedge* electrode varies in y-direction, while the area of the *strip* changes in x-direction. Finally, the *meander* collects all charge neither dumped on the wedge electrode nor on the strip electrode. Thus, the total amount of charge impinging on the anode is

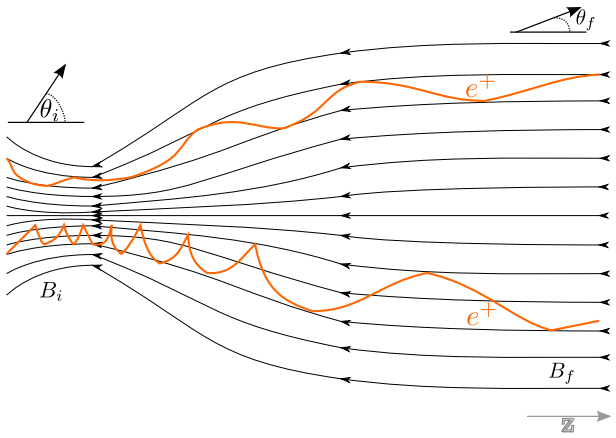

Figure 3.8: Schematic diagram showing the helical motion of a positron in a magnetic field that changes gradually from a strong field B_i to a weaker uniform field B_f, based on Kruit and Read 1983.

known and the position coordinates can be derived through the information of each single electrode:

$$x \propto \frac{Q_s}{Q_{tot}} \qquad y \propto \frac{Q_w}{Q_{tot}}, \tag{3.3}$$

where Q_s is the charge fraction gained through the strip and Q_w through the wedge. Q_{tot} specifies the charge sum allocated by all three electrons.

Similar to the detector using the hexanode, the channel plates of the electron detector have a central hole, but, additionally, the anode - here the wedge-and-strip design - is provided with a cut in the centre. This hole is needed that the projectiles coming from the positron beam line can pass and enter the spectrometer. To realise the hole in WAS, the single electrodes have to be connected in a special way (see figure 3.7). Certainly, the hole in the MCPs and the anode leads to a dead area where no position information can be obtained.

3.2.4 Magnetic beam line transition

As described in section 3.1, positrons from the source are guided magnetically through a beam line from the reactor core to the experimental platform. Therefore, a magnetic field of 6 Gauss is applied by solenoid coils surrounding the beam line tube. However, operating in an optimal range adjusted for the spectrometer a magnetic field strength of one order of magnitude lower compared to the beam line's field is required in the reaction microscope. The weaker, homogeneous B-field of our apparatus is produced by a pair of Helmholtz coils.

In order to overcome the problem of a direct transition from the higher to the lower magnetic field causing unpredictable movement of the projectile particles,

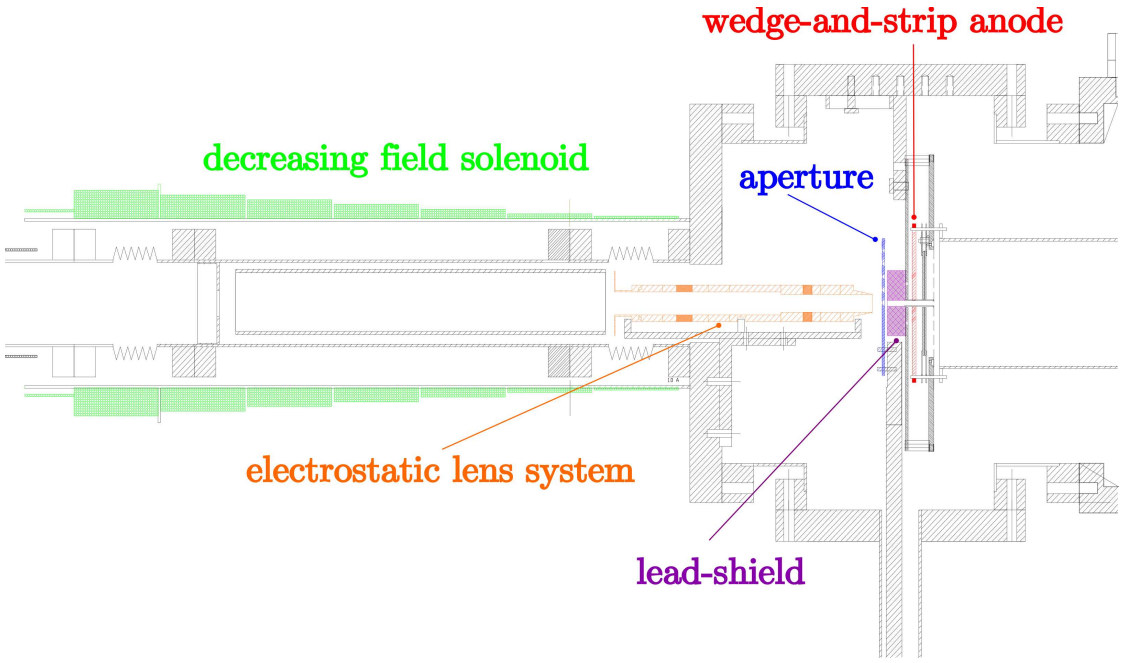

Figure 3.9: Schematic drawing of the used magnetic transition coils. The projectiles are coming from the left side passing the transition field produced by the solenoid, the electrostatic lens system and entering the spectrometer through the aperture, the lead block and the electron detector.

a step-less descent has to be desirable. But, we have to put up with a minimal increase of the beam diameter. The transition is realised by using the properties of an inhomogeneous magnetic field[7] which is implemented over the connection region where the beam line and the main chamber of the reaction microscope are coupled. The variation of this field along the z-axis has to be adiabatic, which means that the field experienced by the positron changes negligibly in course of one revolution of the helical motion. The Lorentz force $q\vec{v} \times \vec{B}$ causes the positrons to spiral around a magnetic field line. They follow it from the beam tube into the spectrometer where the field lines are again parallel due to the uniform field. If the condition of an adiabatic field change is fulfilled the total energy and the classical angular momentum are conserved quantities (see e.g. Jackson 1975). A positron with energy E and velocity v undergoes a helical motion in the beam line's magnetic field B_i because of its non-vanishing velocity component with respect to the z-axis. This induces an angle θ_i between the longitudinal and the transversal velocity component.

[7] Initial studies have been done by Hsu and Hirshfield 1976 and later by Beamson et al. 1980. For a comprehensive overview see Kruit and Read 1983

The angular frequency of a particle's motion is given by:

$$\omega_i = qB_i/m, \tag{3.4}$$

where q and m denote the charge and mass of the positron. The cyclotron radius is

$$r_i = v \sin\theta_i/\omega_i \tag{3.5}$$

and the angular momentum of circular motion is

$$l_i = \frac{m^2 v^2 \sin^2\theta_i}{qB_i} \,. \tag{3.6}$$

The adiabatic field transition implies that the angle θ_f of the helical motion in the spectrometer region where the field B_f is lower and can be expressed by following relation:

$$\frac{\sin\theta_f}{\sin\theta_i} = \left(\frac{B_f}{B_i}\right)^{1/2}, \tag{3.7}$$

resulting in a reduction of the transverse velocity component. Indeed, one derives cooling of this component but nevertheless the total radial size of the projectile beam extends as the positrons follow one magnetic field line. Combination of equations 3.5 to 3.7 gives the ratio of the beam's radius before and after the the transition field

$$r_f/r_i = (B_i/B_f)^{1/2}, \tag{3.8}$$

from which one sees that the magnetic flux enclosed by the orbit is a constant of the motion. Moreover the longitudinal component increases from $v\cos\theta_i$ to

$$v_{f\parallel} = v \cdot \left[1 - (B_f/B_i)\sin^2\theta_i\right]^{1/2} \tag{3.9}$$

since the total velocity is unchanged due to energy conservation. Therefore, the positron trajectories are parallelised as illustrated in figure 3.8[8].

Technically the desired magnetic transition field is achieved by the installation of solenoidal coils around the tube connecting beam line and the experiment. The design of this device is adapted from the principle of a Zeeman slower, introduced by Phillips and Metcalf 1982. Our design (see figure 3.9) features a set of seven coil sections of 40 mm length each along the beam direction, which are wound around a CF63 tube. This tube is mounted over the part where beam line is flanged to the main chamber of the reaction microscope. The coils themselves are made of 1.8 mm diameter wire and consist of 38 windings in the axial direction and 12 (where the field

[8]The effect of parallelisation and unspiralling is also used in an inverse sense, causing in 'magnetic bottle' or 'magnetic mirror' devices. The same effect gives rise to the trapping of electrons in the earth's ionosphere.

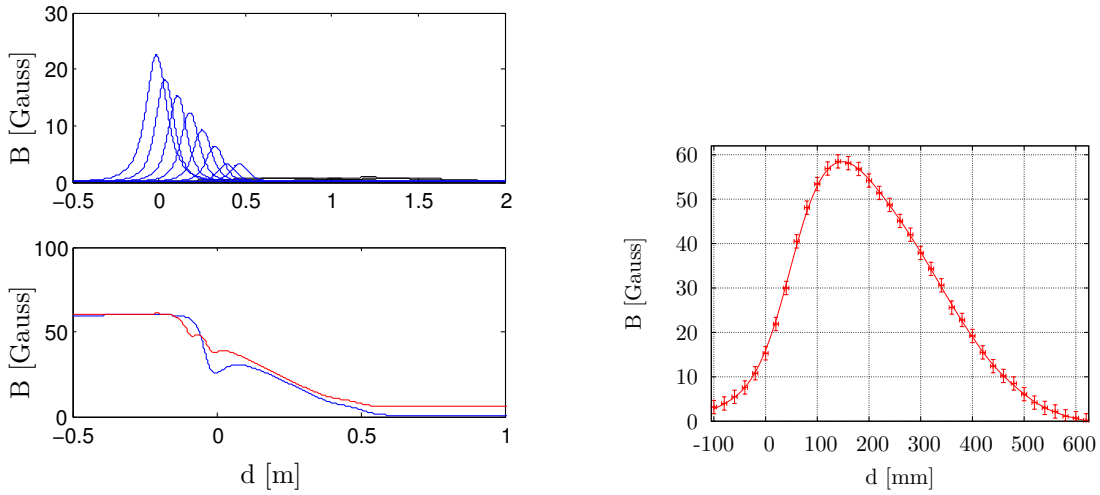

(a) (b)

Figure 3.10: (a) Calculated magnetic field for the transition from the beamline to the reaction microscope. The above plot shows the magnetic field for the individual coils. Figure on bottom represents the field gradient with (red) and without (blue) an additional correction coil. (b) Measured data of the magnetic field gradient in the solenoid tube for all coils performed with the calculated current of 1A.

is highest) to one radial layers of wire. All coil sections are connected and supplied by a current of 1 A. Additionally, in the entrance part of the spectrometer an electrostatic lens system for focussing and deflecting the positron beam is installed. A block of lead is also mounted in front of the electron detector in order to shield the detector from annihilation radiation which occurs when positrons hit material, e.g. by the part of the beam which is cut by an aperture. Detailed description and investigation of a similar set-up was studied in course of a diploma thesis, Spiegelhalder 2005. The performance of our set-up compared to the simulated field gradient is shown in figure 3.10(b).

3.2.5 Data acquisition

Our experiment is operated with a continuous beam of positrons instead of a pulsed beam usually implemented in experiments performed using a reaction microscope. In case of a continuous beam, essential time information are lost due to the missing pulser signal. For the reconstruction of the particles' momentum during the off-line analysis, hence, it is mandatory to find the time origin of the ionising process. Therefore, one has to measure all three particles involved in the reaction where all nine momentum components are measured. Because of the lack of knowledge

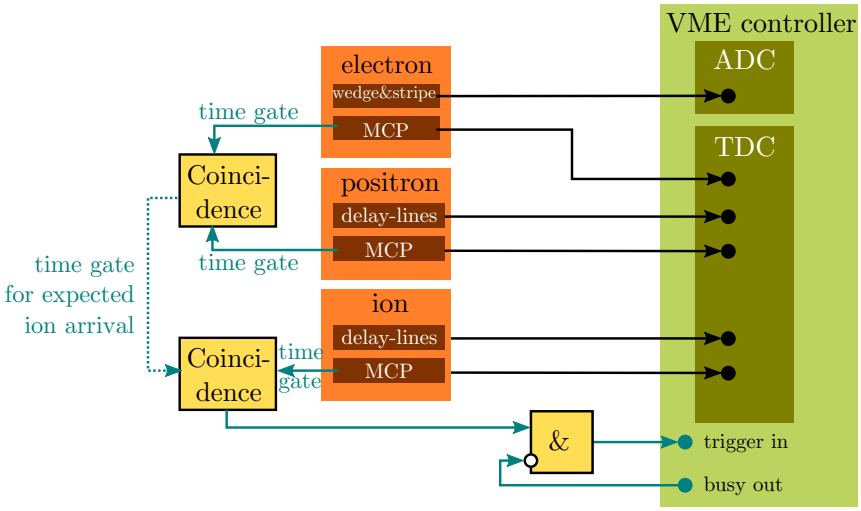

Figure 3.11: Scheme of the used data acquisition system. Positrons and ions are detected one the *same* detector, but for better comprehension separated in the drawing.

for the absolute time information, here, only *triple coincident* events can be taken into account. Consequently, nothing but data sets which correspond to one ionising reaction should be recorded in order to get rid of all useless background data. The data acquisition system which applies conditions on the particles' time-of-flights to get data sets of exactly one ionisation event is schematically shown in figure 3.11. The continuous projectile beam produces consecutively events but a starting point is required for data recording. Therefore, every time a particle hits the *positron/ion* detector or the *electron* detector, a time gate of 1 μs is opened by the hit for the particular detector. This is done because one does not know whether the scattered positron or the ejected electron arrives first on its detector as the particles' time-of-flight depend on the momentum gained in the reaction. If the time gates overlap, which indicates that a coincident event between both detectors is registered, 14 μs[9] later, another time window with a width of 1 μs is opened for MCP signals coming from the *positron/ion* detector. If within this time period a hit - which is treated as a ion impinged on the delay-line anode - is detected, this triple coincident event is chosen to be a "'true"' result of the ionisation. Otherwise theses events can be discarded and the measurement starts again with the incidence of a positron-electron-coincidence. Accidentally, non-coincident events might be recorded leading to high background signals which have to be eliminated during the analysis procedure (see chapter 4).

When a particle hits a detector a signal in the MCP is produced by the emerged electron cloud. This signal is first amplified by a fast amplifier (FA) and afterwards

[9]These 14 μs correspond to the lower limit for the expected ion's time-of-flight.

handled by constant fraction discriminator (CFD) converting it to a standardised NIM-pulse. This time information is then sent to a channel of a multi-hit time-to-digital converter (TDC). The position information for positrons and ions are obtained by the same hexanode. Here, the avalanche of secondary electrons from the MCP deposits its charge on wires of the delay-line anode. These pulses are dispatched to differential amplifiers (DA) and subsequently to CFDs. Those signals containing the position informations from the hexanode are fed directly to the TDC. The electrons' position information is obtained not by a hexanode but by a wedge-and-strip detector. The three signals gained by the three electrodes are first sent to a charge amplifier (CA) which provides a voltage proportional to charge at the input. These signals are further treated in an amplitude-to-digital converter (ADC). The TDC and ADC are controlled by a VME bus system which delivers the acquired data from both detectors via a MBS stream sever to a computer. This VME controller is triggered by the valid coincidence in order to record all times since the beginning of the particular event. Otherwise the memory is clear after a certain time frame.

4 Data analysis

This chapter describes the signal and data processing until the complete momentum vectors for all three particles are obtained. The main analysis routine is performed automatically by the program presented in section 4.1. Therefore, the signals from the detectors have to be read out and converted into position and time information (section 4.2). Using this information, the momentum of each fragment is calculated (section 4.3). Since our experiment is delivered by a continuous projectile beam, the reactions' time origin has to be found. The applied method for its reconstruction is then introduced in section 4.4 which leads finally to fully differential cross sections. Furthermore, the presented approach for a continuous projectile beam has been validated by the employment of a benchmark test using data of a former electron impact experiment (section 4.4.4). Additionally, the acceptance and resolution of the experimental set-up are considered and discussed (section 4.5).

4.1 Data processing and diagnostics

In a conventional (e,2e) spectrometer for this kind of experiments the fully differential cross section (FDCS) is directly proportional to the coincidence count rate of two electrostatic electron electron spectrometers positioned under particular angles which in the course of the measurement are scanned (compare figure 2.3). In contrast, with a reaction microscope FDCS's are not accessible instantaneously. Using a reaction microscope, first all measured data representing each particle's position and time are collected and later reconstructed during off-line analysis. Therefore, beside the experimental execution, in the same way considerable effort has to be put into computer based data evaluation. In order to handle the huge amount data events accumulated during the beam time, a custom-built program is used.

Briefly, the computer-aided system depends on two main platforms: The *ROOT* environment which is an *object-oriented program* (*OOP*) and library written in C++ and developed by CERN (see Brun and Rademakers 1997). Self-built software to analyse a great number of data sets in a very efficient way can be developed with ROOT. The second tool is an other object-oriented C++-framework called *Go4* (see Adamczewski et al. 2004) which uses ROOT as base layer, but additionally extended by a graphical user interface. Programs implemented with ROOT and Go4 can be applied for both real-time monitoring during the experiment and the data analysis afterwards.

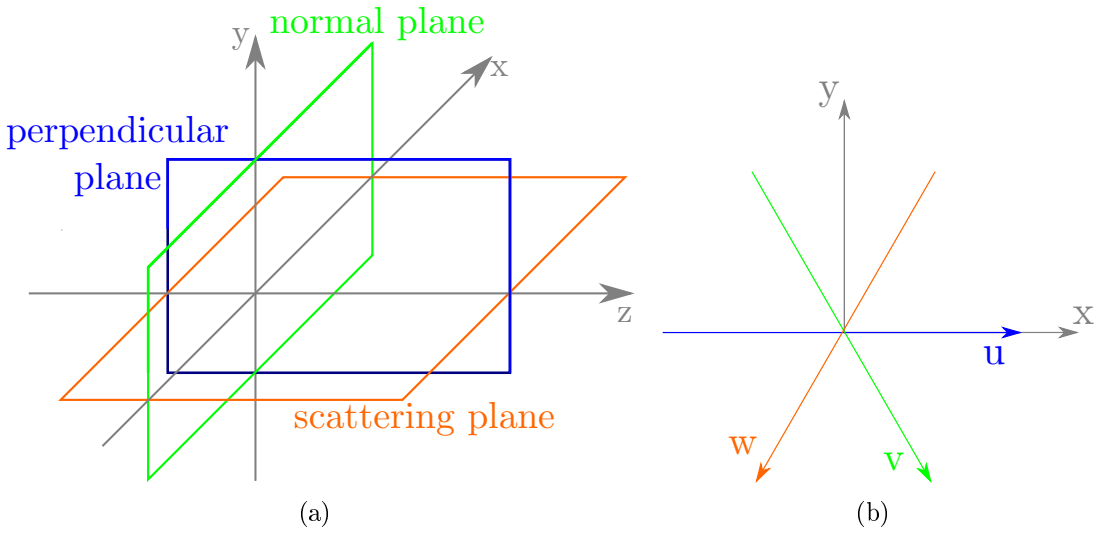

Figure 4.1: (a) Particular planes used in scattering studies. (b) Details on the coordinates u, v, w of the hexanode and the spatial Cartesian coordinates x, y.

The custom-made application used in this work and especially designed for experiments with a reaction microscope is the 'Grand unifiEd reactioN microscopE souRce Code', abbreviated *GENERiC*. GENERiC was introduced initially in Senftleben 2009 where a more detailed review is given. Summarily , the GENERiC analysis program is split into three steps which can be operated sequently or separately where the output of the previous step serves as input for the following one. At the beginning, the TDC raw data are fed into the first step - the `Unpack` step - either directly from the experiment via the MBS stream server or from recorded data files. Here, the untreated data are converted into proper position and time-of-flight informations (see4.2) and sent to the `Analysis` step. As result of the `Analysis` phase, three dimensional momentum vectors for each particle are obtained. The methods used to calculate the momenta, especially the parts which are devised during this work, are further described in section 4.3. The momentum components are stored as vector in cylindrical coordinates, leading to p_z, p_r and ϕ. Thus, the fragments' momenta can be transformed into any required coordinate system. In the final `FDCS` step the momentum data are converted into fully differential cross sections which can be examined then in different planes (compare figure 4.1(a)). The definition and detailed description of the various planes are given in section 4.5 of Senftleben 2009 and therefore omitted here. Moreover, GENERiC features more useful tools, such as easy configuration during run time, special export scripts for histograms, implementation of abstraction concepts typical for OOP and many more[1]. In order

[1]Again, the comprehensive study concerning GENERiC in Senftleben 2009 is recommended.

to sort out useless data or to filter background noise from correct signals, a range of conditions can be applied in the GENERiC code. This feature was very beneficial in a way that a lot of background signals could be suppressed and triple coincident events selected which was necessary for further data handling. In chapter 5 we go into detail regarding this aspect.

4.2 Conversion of the detectors' signals

As a first step, the raw data from both detectors, the hexanode and the wedge-and-strip detector, have to be transformed into position information for further data analysis. The different ways for the hexanode and the WSA are explained briefly in the following subsections.

4.2.1 Position decoding for the delay-line detector

When a particle impinges on the hexanode detector this event has to contain at least one MCP signal and two pairs of signals from the delay-line wires in order to be able to gain position and time information for this hit. The hexanode tends to deliver false or incomplete data sets which leads to loss of data. Due to factors like the low beam intensity and the restricted beam time compared to an electron impact experiments, it is important for positron impact measurements to obtain as much events as possible to achieve the statistical significance, especially for FDCS. Therefore, valid events have to be filtered out and incorrect ones should be reconstructed where possible.

For a hexanode, in a first step, a check on the condition for the time-sum t_{sum} is applied. It is based on the fact that t_{sum} is constant for each layer:

$$t_{sum} := t_1 + t_2 - 2 \cdot t_0 \stackrel{!}{=} const. \tag{4.1}$$

where t_1 and t_2 are the arrival times of the delay-line signal at each end of the wire and t_0 is the time when the particle is registered by the MCP. This condition counts globally for all hits independent of the particle's time-of-flight which is necessary for our experiment since no absolute times are available at this stage of the analysis. Hence, only those events which fulfil this condition are considered to be valid and processed further. In addition, the fact of the constant time-sum is used to reconstruct signals that have not been recorded properly caused by background signals or signals recorded in a wrong order. Furthermore, missing signals either on the MCP or on one end of a delay-line wire can be reconstructed during the `Unpack` step of the program. The consequence of the applied, sophisticated reconstruction routines have been studied extensively in Dürr 2006.

In order to retrieve the (x,y)-value for an incident, one has to take in to account the

three coordinates u, v and w which are provided by the hexanode. The arrangement of the coordinates is illustrated in figure 4.1(b). Thus, the Cartesian coordinates x and y can be determined by following combinations of the hexanodes' coordinates:

$$\begin{aligned} x_{uv} &= u \\ y_{uv} &= \frac{1}{\sqrt{3}} \cdot u - \frac{2}{\sqrt{3}} \cdot v \end{aligned}$$

$$\begin{aligned} x_{uw} &= u \\ y_{uw} &= -\frac{1}{\sqrt{3}} \cdot u - \frac{2}{\sqrt{3}} \cdot w \end{aligned} \tag{4.2}$$

$$\begin{aligned} x_{vw} &= v - w \\ y_{vw} &= -\frac{1}{\sqrt{3}} \cdot (v + w). \end{aligned}$$

The final (x,y)-values are calculated by the combination of the position information from equation 4.2 leading to the localisation of the positrons' and ions' impact position on the detector.

4.2.2 Position decoding for the wedge-and-strip detector

In contrast to a delay-line anode based detector, the position information of a detector using a wedge-and-strip anode can be received with a less demanding read out system and analysing routines. In this case, the position of the Cartesian coordinates x and y can be calculated from the charge ratios between the different electrode segments of the WSA. The dependencies of coordinates and charges are already given in equation 3.3. The position resolution is directly proportional to the achieved signal to noise ratios. Indeed, scale factors are also applied to calibrate the generated image to the physical size of the detector. Further improvements can be achieved by the application of the so-called *cross talk* compensation algorithm[2] which results in a comfortable position decoding and round and linear image.

4.3 Momentum reconstruction

Using a reaction microscope, the complete kinematic information of the ionisation process can be obtained. But so far, we have only the particles' position on the detectors (x,y) and time-of-flight t. The way how the individual three-dimensional

[2]The cross talk routine has been implemented according to RoentDek 2002.

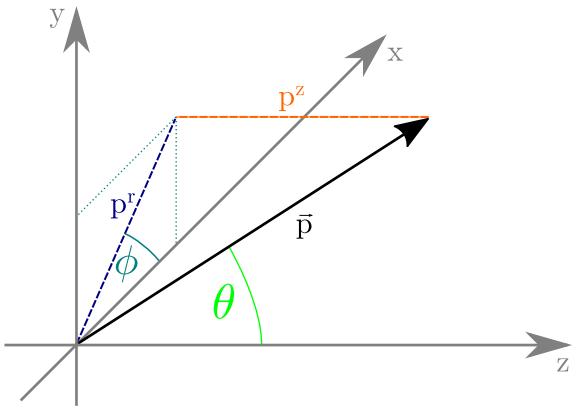

Figure 4.2: Geometry of the momentum components in respect to the Cartesian coordinate system introduced in figure 3.4.

momentum vectors $\vec{p}$ of each fragment is reconstructed with the informations provided by the reaction microscope is described in this section. However, the absolute time-of-flights have to be known for the finding of the correct momentum. As mentioned earlier, the absolute time-of-flight is not accessible apparently for an experiment using a low energetic continuous beam instead of a pulsed one. For a continuous beam also the time origin of the reaction has to be reconstructed which then provides an absolute time scale. As this is one of the main purposes of this work, the method of finding the absolute times is discussed separately in more detail in section 4.4. Hence, in the following it is assumed that a correct time-of-flight for each particle is already retrieved.

The reconstructed complete momentum vectors are expressed in cylindrical coordinates since the spectrometer and the detection set-up implies cylindrical symmetry (compare figure 3.4). The situation is visualised in figure 4.2. Therefore, the longitudinal momentum component is represented by p^z, while the azimuthal angle is denoted as $\phi := \arctan(p^x/p^y)$ and the radial component is given by $p^r := \sqrt{p^{x2} + p^{y2}}$. The particles' *longitudinal* movement along the z-axis is influenced only by the applied electric field in the spectrometer in contrast to the *transverse* motion which is only affected by the magnetic field. The following considerations are appropriate for all kind of particles evolved in the fragmentation process.

4.3.1 Longitudinal momentum

A particle's time-of-flight from the interaction volume to the detector along the z-axis of the spectrometer can be derived simply from Newton's equation of motion (see Fischer 2000). Taking into account the geometry of the spectrometer with the acceleration length l_a where the electric potential U is applied and the drift length l_d, the time-of-flight for a particle with mass m, charge q and an initial longitudinal

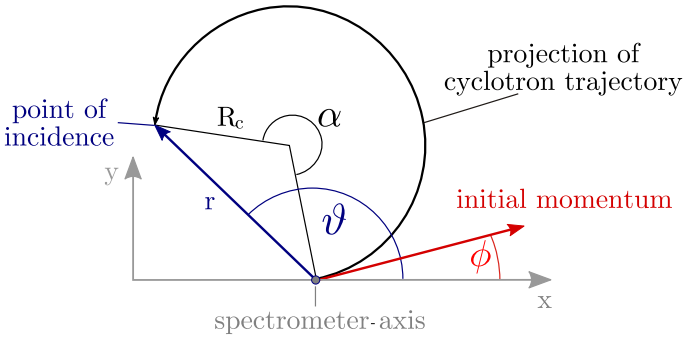

Figure 4.3: Reconstruction of the momentum's transverse component p^r.

momentum component p_z can be expressed as:

$$t(p^z) = m \cdot \left(\frac{2l_a}{\sqrt{p^{z2} + 2mqU} \pm p^z} + \frac{l_d}{\sqrt{p^{z2} + 2mqU}} \right), \tag{4.3}$$

where the "+" sign is used when the particle is accelerated in $+z$-direction and "−" otherwise. The product qU is positive for both positively and negatively charged fragments.

There exists no analytic inverse function for equation 4.3 , therefore, a numerical approach has to be employed to find the initial longitudinal momentum p^z for a measured time-of-flight t. For each particle this is done using Newton's method[3] to find a root of the function $f(p^z) = R(p^z) - t$ where $R(p^z)$ denotes the right-hand side of equation 4.3. For the particular case of a particle's momentum reconstruction a summary of the numerical details and its implementation in GENERiC can be found in appendix B of Senftleben 2009. In there, it is also demonstrated that due to the strict monotonicity of $f(p^z)$ the right value of p^z is always gathered from the algorithm[4].

4.3.2 Transverse momentum

With its time-of-flight and position information also each particle's transverse momentum can be calculated. Here, one takes advantage on the fact that the charged fragments are forced onto a cyclotron motion while travelling to the detectors. This cyclic trajectory results from the magnetic field B_z applied in parallel to the spectrometer axis while its revolution's frequency is given by

$$\omega_c = \frac{|q|B_z}{m}. \tag{4.4}$$

[3]See appendix A for a brief introduction of Newton's method.
[4]This conclusion is valid for the momentum range of interest.

Its radius R_c depends only on the initial momentum $p^r = \sqrt{p^{x2} + p^{y2}}$ perpendicular to the z-axis (compare figure 4.3)

$$R_c = \frac{p^r}{\omega_c}. \tag{4.5}$$

As illustrated in figure 4.3, R_c is not accessible directly through measurement, instead, the observables which can be processed are the radius r on the detector and the angle α. It is given by $\alpha = \omega_c \cdot t$ specifying the angle between the start point and the final position on the detector of the particle's way through the spectrometer projected on the xy-plane of the trajectory. Using these two observables, the cyclotron radius can be derived from the following equation:

$$R_c = \frac{r}{2|\sin(\frac{\alpha}{2})|}, \tag{4.6}$$

which allows to calculate the magnitude of the transverse momentum with equation 4.5

$$p^r = \frac{r \cdot m \cdot \omega_c}{2|\sin(\frac{\omega_c t}{2})|}.^{5} \tag{4.7}$$

Finally, the azimuthal angle $\phi = \arctan(p^x/p^y)$ missing to complete the initial momentum vector of a particle can be expressed as

$$\phi = \vartheta \pm \frac{\omega_c t \pmod{2\pi}}{2} \tag{4.8}$$

where ϑ is the polar angle in the detector plane. In our set-up, positively charged fragments take a clockwise turn, therefore the "+"-sign is used. Accordingly, particles with a negative charge move anti-clockwise and the "−"-sign has to be applied in order to retrieve ϑ.

4.4 Reconstruction of the reaction's time origin

While the time-of-flight measurement normally requires a pulsed projectile beam and a synchronous train of time-marker signals, such a pulsed beam is not applied in the present experiment with the positrons from the NEPOMUC facility. It is not feasible as using a pulser would decrease the already quite low reaction rate even more. Therefore, we have to come to terms with a continuous flux of positrons during the limited beam time at FRM-II in order to collect enough event counts for statistically meaningful cross sections. Therefore, we have to deal with the disadvantage that the absence of a pulser signal suffers the loss of an absolute time.

[5] Equation 4.7 is valid for all kind of particles as demonstrated in Senftleben 2009, p 58

In the present experiment the full kinematics have to be obtained using the redundant information from the detection of all continuum particles in combination with their relative time differences and momentum conservation. For the reconstruction of the particle's initial momentum as described in the previous section 4.3 it is sufficient to know the point in time when the process of ionisation took place. In common (e,2e)-experiments with a pulsed electron beam, the time origin can be determined taking advantage of the *wiggle*-structure which appears when the radius r of the electrons is plotted against their total time-of-flight t_{total} starting from the last projectile pulse until the incidence on the detector[6] (compare figure 4.8). But since this feature is not available in our experiment, a different approach has to be taken into account to find the particles' time-of-flight.

4.4.1 Method used for a continuous beam

Due to the missing pulser signal there is a lack of a defined start point for the measurement, but with the applied data acquisition system we are able to obtain the time difference Δt between the various hits on the detectors. These will be identified by subscript indices, e.g. $\Delta t_{\mathrm{e^-ion}} = t_{\mathrm{e^-}} - t_{\mathrm{ion}}$ represents the time difference between the impingement of the electron on the detector and the detection of the ion's impact. With the use of $\Delta t_{\mathrm{e^+ion}}$ and $\Delta t_{\mathrm{e^+e^-}}$ only the positron's time $t_{\mathrm{e^+}}$ from the collision to the detector is undetermined. Since the electron's and ion's time-of-flight can be calculated with their time references to the positrons' detection: $t_{\mathrm{e^-}} = \Delta t_{\mathrm{e^+e^-}} + t_{\mathrm{e^+}}$, $t_{\mathrm{ion}} = \Delta t_{\mathrm{e^+ion}} + t_{\mathrm{ion}}$. Comparable to the calculation of the particles' individual longitudinal momenta, the positron's time-of-flight is reconstructed using Newton's method but in a different approach.

Considering an ionisation event as given in expression 2.3, there are three particles in the continuum: the scattered positron, the electron ejected from the atom and the residual ion. Due to momentum conservation, the sum of all final state momentum vectors $\vec{p}_{sum}$ has to be equal to the initial projectile momentum $\vec{p}_0 = (0, 0, p_0^z)$:

$$\vec{p}_{sum} = \vec{p}_{\mathrm{e^+}} + \vec{p}_{\mathrm{e^-}} + \vec{p}_{\mathrm{ion}} \stackrel{!}{=} \vec{p}_0. \tag{4.9}$$

Furthermore, the relative time differences when these fragments are detected is known. Thus, all longitudinal momenta can be written as a function[7] of the positron's time-of-flight $t_{\mathrm{e^+}}$: $p^z_{\mathrm{e^+}} = f(t_{\mathrm{e^+}})$, $p^z_{\mathrm{e^-}} = f(t_{\mathrm{e^+}} + \Delta t_{e^+e^-})$ and $p^z_{\mathrm{ion}} = f(t_{\mathrm{e^+}} + \Delta t_{\mathrm{e^+ion}})$ since $t_{\mathrm{e^-}} = t_{\mathrm{e^+}} + \Delta t_{\mathrm{e^+e^-}}$ and $t_{\mathrm{ion}} = t_{\mathrm{e^+}} + \Delta t_{\mathrm{e^+ion}}$. The subscript denotes which particle is regarded and the time intervals $\Delta t_{\mathrm{e^+e^-}}$ and $\Delta t_{\mathrm{e^+ion}}$ are given for a certain reaction. Finally, the sum of all longitudinal momenta in the final state p_{sum}

[6] Refer to Senftleben 2009, p 56 for a detailed description of this procedure.

[7] This function is indeed the inverse function of $t(p^z)$ (see equation 4.3), since p^z can be expressed as function t accordingly.

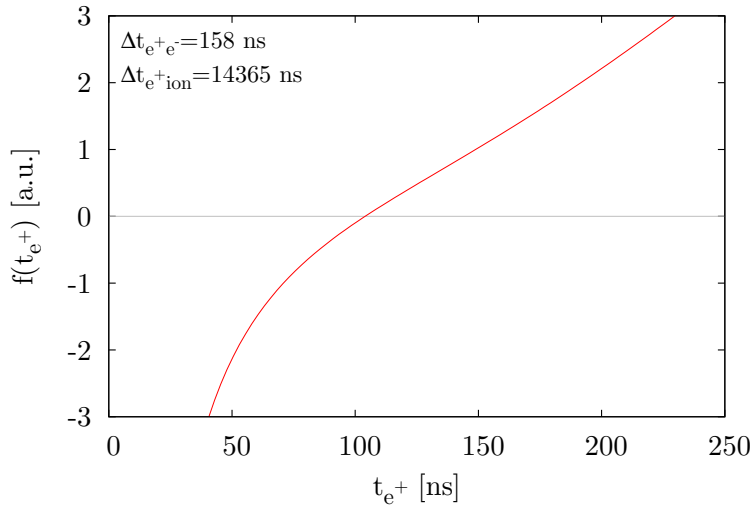

Figure 4.4: $f(t_{e^+})$ plotted over the desired momentum range while $\Delta t_{e^+e^-}$ and Δt_{e^+ion} represent some typical values for these time differences.

depends on the time which takes the positron to travel from the reaction point to the detector.

Through the alignment of the projectile beam along the spectrometer axis, the transverse momenta of the three particles involved in the reaction are balanced resulting in a vanishing net transverse momentum. Thus, only the longitudinal momenta have to be regarded:

$$p_{sum}(t_{e^+}) = p^z_{e^+}(t_{e^+}) + p^z_{e^-}(t_{e^+} + \Delta t_{e^+e^-}) + p^z_{ion}(t_{e^+} + \Delta t_{e^+ion}) \stackrel{!}{=} p^z_0 \tag{4.10}$$

Since the momentum in z-direction for each fragment can be obtained as described in section 4.3.1 and since the sum of all particles' momenta in the final state must be equal to the projectile's initial momentum, the finding of t_{e^+} is reduced to the determination of the root of the following expression:

$$f(t_{e^+}) = p^z_0 - p_{sum}(t_{e^+}). \tag{4.11}$$

This root can be calculated using the iteration formula of Newton's method which in our case to leads to:

$$t^{(k+1)}_{e^+} = t^{(k)}_{e^+} - \frac{f\left(t^{(k)}_{e^+}\right)}{f'\left(t^{(k)}_{e^+}\right)}. \tag{4.12}$$

This algorithm should converge to the wanted time-of-flight for the scattered

positron, but the convergence is not guaranteed in general. Furthermore, the behaviour of this iteration has to be verified for the specific terms of our case. As illustrated in figure 4.4 for a particular case of $\Delta t_{e^+e^-}$ and Δt_{e^+ion} , $f(t_{\mathrm{e}^+})$ is strictly monotonic over the considered time interval for the momentum range relevant for the experiment. Hence, there is only one root which represents the solution to our problem . The iteration is aborted when either the value of the current function $|f(t_{\mathrm{e}^+}^{(k)})|$ or the difference between two consecutive points $|t_{\mathrm{e}^+}^{(k+1)} - t_{\mathrm{e}^+}^{(k)}|$ is arriving below a preset threshold. Within the implemented code also a limit to the number of iteration steps is set as further break condition in order to prevent the algorithm from the possibility of not stopping. The actual implementation is discussed in the appendix A.2 where also the developed C++ code in GENERiC is shown (see listing A.1).

4.4.2 Obtaining the momentum sum and its derivative

As one can see in equation 4.12, the knowledge of the final momentum sum and its derivative is imperative. The sum of the three particles' longitudinal momenta in the final state is gained by the numerical approach described in section 4.3.1. However, in order to get the derivative of this function for each fragment, we need to know the inverse function to equation 4.3. But as already mentioned, there is no analytic way to retrieve the inverse, so different approximative approaches have to be used.

Due to the ion's higher mass[8] and the resulting small kinetic energy compared to its energy gained by the electric potential of the spectrometer, equation 4.3 can be approximated by a Taylor expansion around $t(p^z = 0)$. While neglecting terms of higher order, the expansions finally delivers:

$$t(p^z)|_{p^z=0} \simeq \frac{l_{a+} + l_{d+}}{2}\sqrt{\frac{2m_i}{q_i U_i}} - \frac{l_{a+}}{q_i U_i} \cdot p^z + \mathcal{O}(p^{z2}), \tag{4.13}$$

which leads to an expression for the ion's longitudinal momentum

$$p^z_{\mathrm{ion}}(t_{\mathrm{e}^+}) = \frac{q_i U_i}{l_{a+}} \cdot \left(\frac{l_{a+} + l_{d+}}{2}\sqrt{\frac{2m_i}{q_i U_i}} - (t_{\mathrm{e}^+} + \Delta t_{\mathrm{e}^+\mathrm{ion}}) \right), \tag{4.14}$$

where it only depends on the positron's time-of-flight. Then, the derivative of p^z_{ion} with respect to t_{e^+} is given by following constant:

$$\frac{d\, p^z_{\mathrm{ion}}}{dt_{\mathrm{e}^+}} = -\frac{q_i U_i}{l_{a+}}. \tag{4.15}$$

[8] The singly charged helium ion has more than 7300 times the mass of the leptons involved in the reaction, the positron and the electron. But the obtained momenta are comparable in magnitude.

The situation for the lighter fragments, namely the scattered positron and the rejected electron, is more complicated as equation 4.3 can no longer be approximated sufficiently by a linear function. Instead the longitudinal momentum for both leptons can be extracted using a approximative formula. Therefore, two substitutions have to be done

$$T_e := \frac{t_e\sqrt{q_e U_e}}{l_a\sqrt{2m_e}}, \quad X_e^2 := \frac{{p_e^z}^2}{2m_e q_e U_e}, \tag{4.16}$$

here the subscript "e" stands for either the electron or its antiparticle, the positron. In order to set these substitutions, we have to assume that $l_d = 2 \cdot l_a$ which is fulfilled in our case. As result of the transformation, equation 4.3 now reads:

$$T_e = \frac{1}{\sqrt{1 + {X_e}^2} + X_e} + \frac{1}{\sqrt{1 + {X_e}^2}}. \tag{4.17}$$

Thus, the inverse can be approximated using

$$X_e = A_e + \frac{B_e}{T_e} + C_e \cdot T_e + D_e \cdot \sin(T_e) \tag{4.18}$$

whereas the constant parameters A_e, B_e, C_e and D_e are determined for the positron and the electron respectively by fitting this function[9]. In our case, the fit leads to following values: $A_{e^+} = -0.051$, $B_{e^+} = 1.601$, $C_{e^+} = -0.430$ and $D_{e^+} = 0.378$ for the positrons and $A_{e^-} = 0.095$, $B_{e^-} = -1.533$, $C_{e^-} = 0.462$ and $D_{e^-} = -0.307$ for the electrons. With equations 4.16 and 4.18 the longitudinal momentum for the positron and the electron can be written

$$p_e^z = X_e \cdot \sqrt{2m_e q_e U_e}. \tag{4.19}$$

Through this approximative method one obtains the derivative of p_e^z

$$\frac{d\,p_e^z}{dt_e}(t_e) = 2m_e\,\kappa_e \cdot \left((-B_e\,l_a/\kappa_e \cdot t_e)^2 + C_e\,l_a\,\kappa_e + D_e\,l_a\,\kappa_e \cos\left(\,l_a\,\kappa_e \cdot t_e\right)\right), \tag{4.20}$$

where the abbreviation $\kappa_e = \sqrt{(q_e U_e)/(2m_e)}$ is applied.

Finally, with the derivatives of the longitudinal momenta of all fragments the derivative needed in equation 4.12 is accessible and can expressed as

$$f'\left(t_{e^+}^{(k)}\right) = -\left(\frac{d\,p_{e^-}^z}{dt_{e^+}}\left(t_{e^+}^{(k)}\right) + \frac{d\,p_{e^+}^z}{dt_{e^+}}\left(t_{e^+}^{(k)}\right) + \frac{d\,p_{e^{\mathrm{ion}}}^z}{dt_{e^+}}\left(t_{e^+}^{(k)}\right)\right), \tag{4.21}$$

where the "$-$" sign comes from the convention that the momentum sum is subtracted

[9] The fitting is done using the least-square fit algorithm of *gnuplot*, e.g. see Kelley 2007 or Janert 2007. A concise reference of non-linear least-square fits is given in Press 2007, chapter 15.

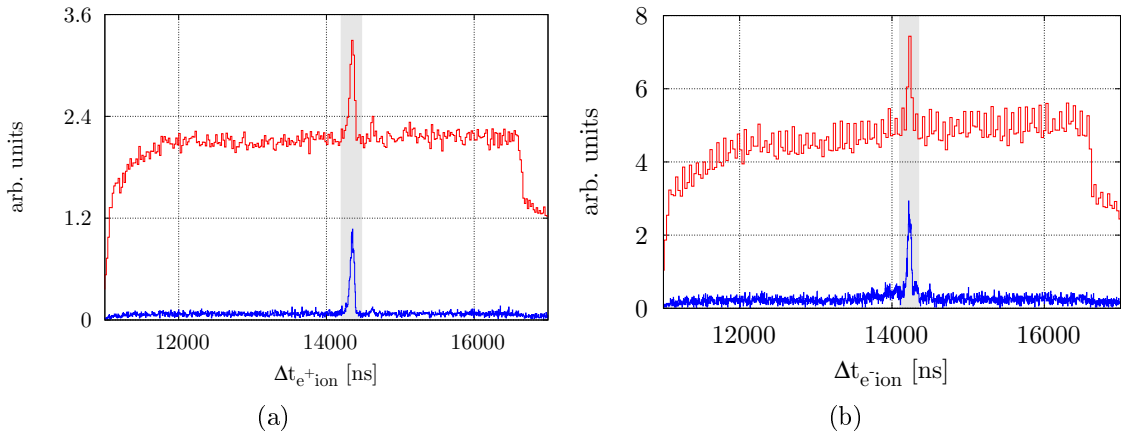

Figure 4.5: Time difference spectra: (a) $\Delta t_{e^+\text{ion}}$ (b) $\Delta t_{e^-\text{ion}}$. The red lines show the spectra of the raw data; the blue lines are used for the spectra with the condition on the ion's position.

from the projectile momentum in equation 4.11. Now, using this method, it is possible to retrieve an absolute time for each reaction with the knowledge of the initial projectile momentum and the time difference between the fragments.

4.4.3 Triple coincident events

An event, coming from the data acquisition system, should be a result of an ionisation reaction according to equation 2.3, where the three fragments are detected in coincidence. However, due to the very high signal rates on both detectors caused by annihilation radiation, we get high background signals on our detectors. This leads to a huge amount on events which do not originate from ionisation but caused by false hits when the time gates for data acquisition are opened (see also section 3.2.5). For further data analysis, one has to get rid of all those false events and identify triple coincident events which originate from an ionisation process.

In the time difference spectra where the time difference between the positron and the ion hit on the detector $\Delta t_{e^+\text{ion}}$ and time difference between the electron and the ion impact on the detector $\Delta t_{e^-\text{ion}}$, peaks occur which indicate a correlation between the hits (compare figure 4.5). In these histograms, the high background signals are visible. If we now select events which are registered within a small time window around the peaks in the time difference spectra (shaded grey in the figures 4.5) and plot the position of the ions for this specific event, we receive the position picture shown in figure 4.6(b). Compared to the detector picture without these conditions applied (figure 4.6(a)), one can clearly identify the impact area of the ions on the detector after the elimination of the background. The ion's spot is

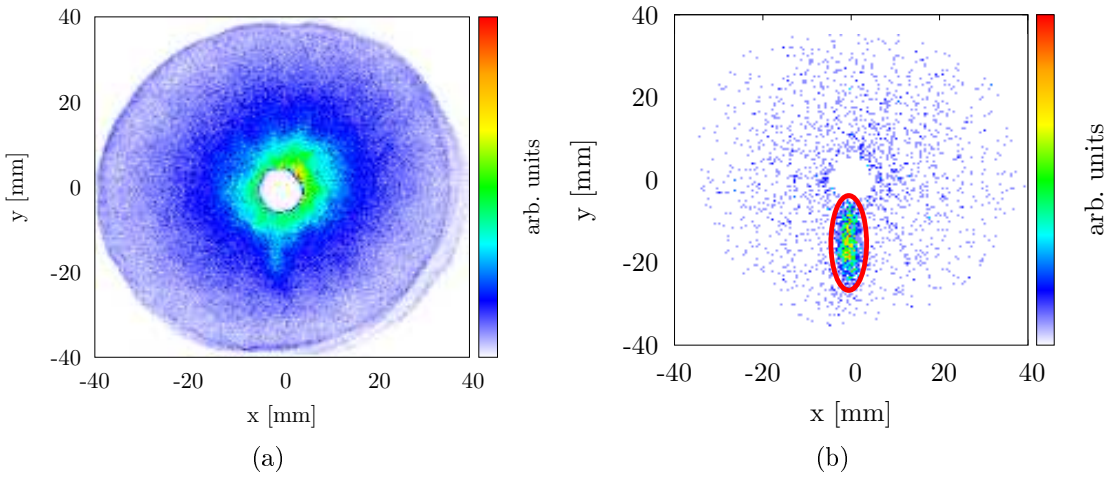

Figure 4.6: The ion's position. (a) raw data for the second hit on the positron/ion detector (b) with condition on time difference. The red framed area shows the events selected for further processing.

expanded in y-direction resulting from the initial momentum downwards gained by the supersonic expansion which adds also to the worse resolution in this direction compared to x-direction. Only those events whose ions are located within the spot under the detector's hole are used for further analysis and these are treated as triple coincident events (compare figure 4.6(b)) generated in the ionisation process. In figure 4.5, the time difference spectra are plotted for these "'true"' events in blue where again the decrease in background signals is illustrated. Finally, the positrons' time-of-flight which was reconstructed using the above described method is shown in figure 4.7.

4.4.4 Benchmark test using (e,2e)-data

Due to the fact that we could not proof that the above described approach is correct and delivers appropriate results for our positron data recorded at NEPOMUC, we transferred the method of finding the reaction's time origin to data already obtained through electron impact experiments. Hence, we are able to compare results of a data set[10] analysed by two different way: on one hand the former, common used method of analysis and on the other hand the approach described in this work for a experiment where only time differences are known. Since the amount of data used for this benchmark test is larger then the relevant data collected during the beam time in Munich, analysing these (e,2e)-data is statistically much more significant.

[10]Data from a former experiment of electron scattering on helium with an impact energy of 100eV are used.

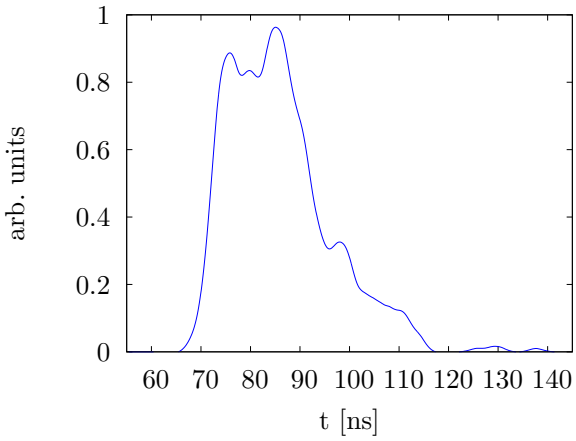

Figure 4.7: The reconstructed time-of-flight t_{e^+} of the positrons.

In order to be able to transfer the results of a former (e,2e)-experiment performed with a pulsed beam to the analysis procedure for a continuous beam, we only used the time difference informations for the three particles - here, two electrons and one ion - and discarded the profitable information of an absolute time gained by the pulser. The regular way of data analysis for a (e,2e)-data set still requires a lot of calibration effort until one gets finally the fully differential cross sections. Despite of the knowledge of an absolute time, plenty of calibration work has to be done taking advantage of momentum and energy conservation. With the calibration procedure, one bypasses the ignorance of the spectrometer's exact geometry and the effective fields within the apparatus. A comprehensive descriptions of finding FDCS for common performed electron impact experiments is given in Dürr 2006 and Senftleben 2009. Here, one also uses parameters which allow to *shift* and *scale* times and momenta until they fit the requirements of the conversation laws without the exact knowledge of the situation in the spectrometer. But these scale and shift factors are obsolete in our case of a continuous beam having this lack in time information. Since it is impossible to determine all criteria which are involved, such as the applied fields, the length for the drift region, the position of the detectors, etc., we rely on parameters which can be adapted until both way of data analysis agree. Therefore, the variation of acceleration length and drift length is executed leading to effective values for those.

In conclusion, we can say that results obtained by the common method could be reproduced with the approach introduced in section 4.4.1 (compare figures 4.8 and 4.9 for some exemplary distributions). Thereby, we additionally gained a better understanding of the working principle for the described way to reconstruct a missing time origin of an ionising reaction. Furthermore, we could point out that it is necessary for further positron experiments to predetermine the geometry for the used set-up accurately in order to identify the effective acceleration and drift length.

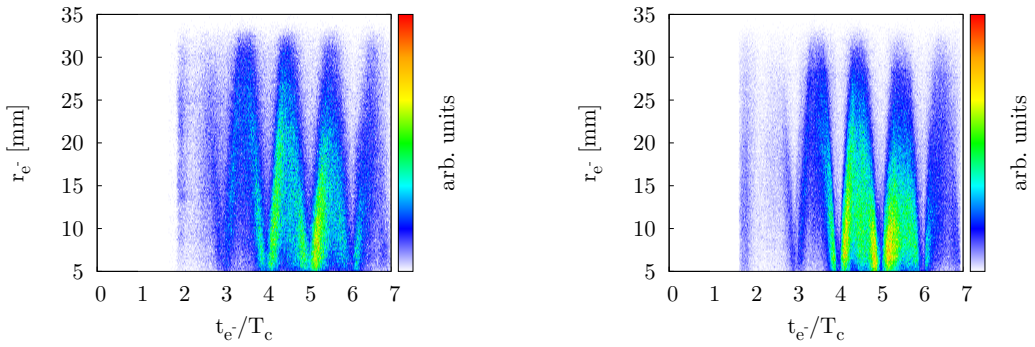

Figure 4.8: The detected radial position r of the electron incidence against the moved portion of the electrons cyclotron trajectory for the (e,2e)-benchmark test. (a) Analysed by the method introduced in this work, (b) analysed in the common way.

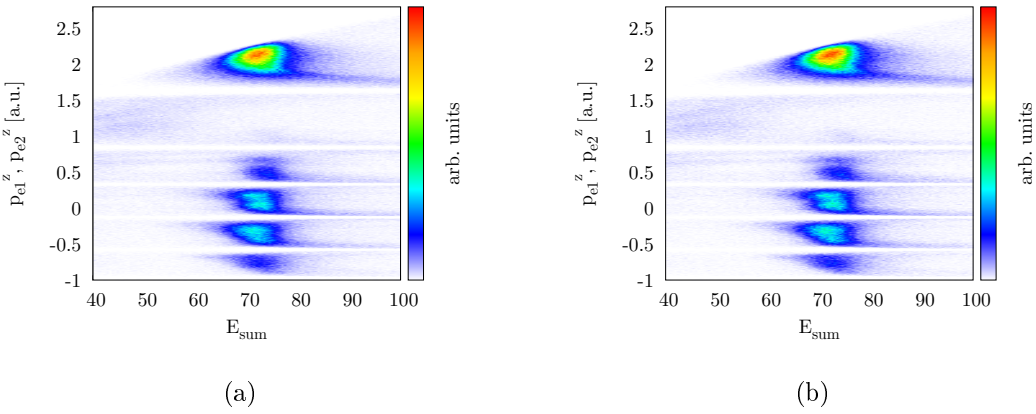

Figure 4.9: Energy sum against the individual longitudinal momenta of the final sate electrons (1) and (2) for the (e,2e)-benchmark test. (a) Analysed by the method introduced in this work, (b) analysed in the common way.

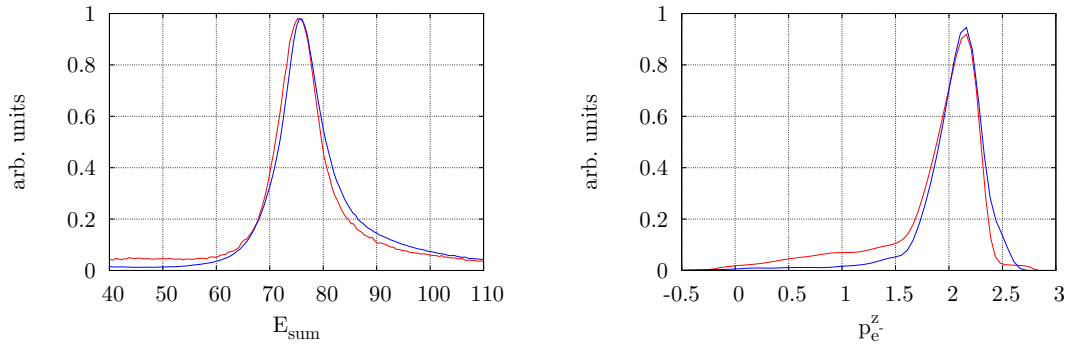

(a) (b)

Figure 4.10: Comparison of (a) the energy sum, (b) the first electron's longitudinal momentum. Both histograms made for the (e,2e)-benchmark test data. The red lines indicate the result obtained by the approach introduced in this work and the blue lines are used for the results analysed with common way.

4.5 Performance: acceptance and resolution

For a reaction microscope the acceptance is defined by the ranges of solid angle and energy that can be detected. Due to the different mass and energy, the details have to be considered separately for the lighter particles, namely the positron and the electron, and the heavier ion. If a statement is given which can be applied for positrons as well as for electron, we accent it with e as subscript. Whereas the particles' specification e^+ and e^- are used if the two leptons have to be distinguished. Despite of the low statistical significance resulting from the insufficient data set gained in the experiment in Munich, the way of obtaining the spectrometers' resolution is presented and in the case of significant results and reliable limits, they are given.

4.5.1 Acceptance

The momentum acceptance in longitudinal direction for all three fragments is limited by the acceleration voltage U which is applied on the side of the spectrometer opposite to that where the particle is detected. Thus, only those cannot be measured that have a large backward momentum and can overcome this potential. Hence, positrons and ions with $p^z > -\sqrt{2m|qU|}$ and all electrons with $p^z > \sqrt{2m|qU|}$ are detected, resulting in $p^z_{e^+} > -1.03\,\text{a.u.}$ for positrons, $p^z_{e^-} < 2.26\,\text{a.u.}$ for electrons and $p^z_{\text{ion}} > -88.04\,\text{a.u.}$ for the ions.

In transverse direction the acceptance for the two leptonic fragments is mainly

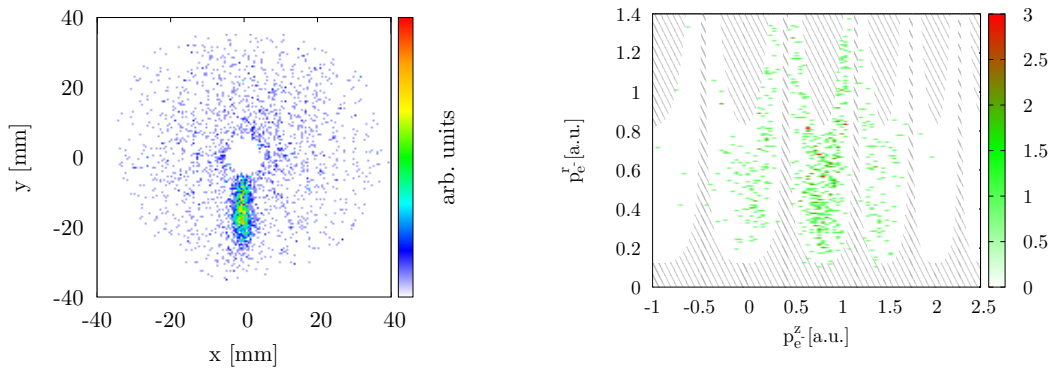

(a) (b)

Figure 4.11: (a) Position of the ions on the detector with conditions on the time difference spectra. The centre of mass for the ions' incidence spot is shifted downwards because of the initial momentum in $+y$-direction introduced by the jet. (b) Detected momentum space for the electrons. Areas with no acceptance are shaded.

governed by the by the size of the MCPs and their holes in the centre. Since the radial extension of their trajectories is confined by the magnetic field (compare figure 4.3), the detection is restricted within a certain range. Therefore, the minimal (maximal) transverse momentum for positrons and electrons can be calculated by half the radius of each detectors' hole (of each MCP) using equation 4.6:

$$p^r_{e,min(max)} = R_{e,min(max)} \cdot q_e \cdot B. \tag{4.22}$$

The electron detectors' MCP has a diameter of 40 mm that leads to a maximum radius $R_{e^-,max} = 10\,\text{mm}$ and its hole amounts $R_{e^-,min} = 2.5\,\text{mm}$. For the positrons these values are given by $R_{e^+,max} = 20\,\text{mm}$ and $R_{e^+,min} = 2.5\,\text{mm}$. With the applied magnetic field of $6 \times 10^{-4}\,\text{T}$ we get $p^r_{e^-,min} = 0.12\,\text{a.u.}$ and $p^r_{e^-,max} = 0.48\,\text{a.u.}$ for the electrons' transverse momentum and $p^r_{e^+,min} = 0.12\,\text{a.u.}$ and $p^r_{e^+,max} = 0.96\,\text{a.u.}$ for the positrons, respectively. Furthermore, the acceptance is affected by the cyclotron motion which forces all particles to return onto the spectrometer axis when their time-of-flight is an integer multiple of the cyclotron period T_c. As consequence, if $t_e = n \cdot T_c$, $n \in \mathbb{N}$ is fulfilled for the time-of-flight, these particles cannot be detected because of the hole in the detector. This behaviour is also responsible for the typical *wiggle* structure, as e.g. shown in figure 4.8 for the electrons in the benchmark test. In order to overcame this drawback, the gaps in the acceptance could be filled by performing the experiment for a specific kind of target with different voltages[11]. Subsequently, during the off-line analysis, these independent measurements have to

[11] The combination of several measurement runs has been introduced in Dürr 2006

be combined to cover the complete momentum space. Due to the limited beam time and the prototype character of the positron experiment at NEPOMUC facility, it was impossible to run the experiment with three different voltages. This technique will be applied possibly in future measurements to improve the resulting data.

In order to determine the transverse momentum for the ions, the magnetic field can be neglected, because the heavy ion does perform less than one cyclotron revolution. The minimal and maximal transverse momentum component can be estimated to

$$p^r_{\mathrm{ion},min(max)} = r_{min(max)} \cdot \frac{m_i}{t_{\mathrm{ion}}}, \tag{4.23}$$

whereas we used the equation 4.7 in the limit of large masses. Since a longitudinal ion's momentum of $p^z_{\mathrm{ion}} \approx 0$ can be assumed for the approximation, with the time-of-flight from equation 4.3 one gets finally:

$$p^r_{\mathrm{ion},min(max)} = r_{min(max)} \frac{\sqrt{2m_i q_i U_i}}{(2l_{a+} + l_{d+})}. \tag{4.24}$$

With the same minimal and maximal radius as for the positrons, as both are detected on the same detector, this leads to an upper limit in the transverse momentum of $p_{\mathrm{ion},max} = 9.8\,\mathrm{a.u.}$ and minimal transverse momentum $p_{\mathrm{ion},max} = 2.0\,\mathrm{a.u.}$. But the acceptance region for the ions is shifted by $m_i \cdot v_{jet} = 3.6\,\mathrm{a.u.}$ in $+y$-direction as the ions obtain an initial momentum in from the gas jet (see figure 4.11(a)). This initial shift causes that ions with zero momentum in transverse direction - normally hitting the hole - are guided onto the detector and all ions with $p^r_{\mathrm{ion}} < 7.6\,\mathrm{a.u.}$ can be detected. This applies essentially for all ions produced in the fragmentation process.

4.5.2 Resolution

The spectrometers' momentum resolution is influenced by a couple of parameters. How well do we know the values for the acceleration distances l_{a+} and l_{a-}, the drift lengths l_{d+} and l_{d-}, the acceleration voltages $U_{e^+} = U_i$ and U_{e^-} and the magnetic field B ? There are many uncertainties which could not be eliminated, such as the gradient, the real strength or lensing effects of the applied fields or the exact geometry of the spectrometer. As already mentioned, in common (e,2e)-experiments with a pulsed beam, these factors can be determined by a specific calibration process using additional scaling and shifting quantities. However, in continuous beam experiment with a lack of an absolute time, one suffers the loss of one free parameter which has to be reconstructed in our case. For example, the magnitude of the magnetic field B is accessible easily for the common procedure by evaluating the wiggle structure in the time-of-flight spectrum (compare figure 4.8). Here, having a continuous flow of projectiles, the value for B cannot be found directly, thus we have to enter this quantity as input and obtain the reactions' time origin by the method described

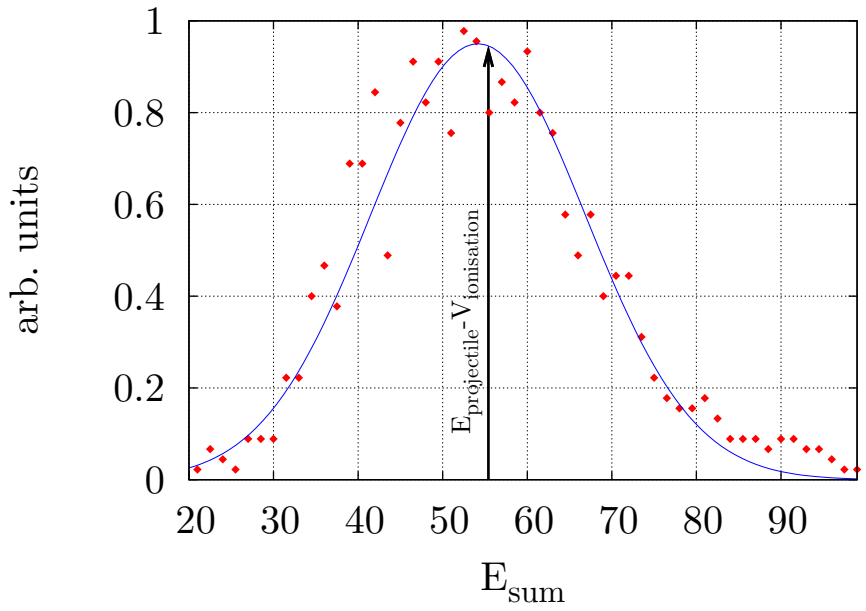

Figure 4.12: Energy sum of the particles in the final state for positron impact ionisation of helium. The arrow indicates the energy $E_{projectile} - V_{ionisation}$ where $E_{projectile}$ is the energy of the incoming projectile and $V_{ionisation}$ denotes the threshold energy of ionisation.

above. As demonstrated in section 4.4.4 the introduced approach works reliable if all quantities are given. For the benchmark test, we first analysed the data in the common approach and then took advantage of the gained knowledge using it as input for the new way of analysis. Doubtless, this way was used for demonstration purpose but could not be applied for the data of the positron experiment. In order to overcome uncertainties of the input parameter, we have to investigate other ways of calibration which are discussed later. Furthermore, we have to take into account that the momentum of the ion with its large uncertainty contributes directly in the calculation of the positrons' time-of-flight (see equations 4.10 - 4.12).

As we do not have any comparison measurement whereof the unknown parameter could be obtained, we have to make some assumptions in order to perform the analysis of the positron data collected at NEPOMUC. Hence, we have to adapt the acceleration and drift lengths - our modifiable parameters - in a way that energy conservation is fulfilled (compare figure 4.10(a)). Since for single ionisation of an atom the initial energy E_0 is shared among the scattered positron and the rejected electron

$$E_0 = E_{e^+} + E_{e^-} + Q, \tag{4.25}$$

where E_{e^+} and E_{e^-} are the positrons' energy and electrons' energy after the collision and Q is the change of internal energy. In our case - single ionisation in the

ground state of He^+ - this is the ionisation potential $Q = V_{ionisation} = 24.6\,\text{eV}$. A proper calibration for our free parameters could be found when the energy sum is independent of transverse and longitudinal momentum of both individual particles. This can be seen in figure 4.9 for the (e,2e)-data used in the benchmark test, but no clear evidence can be made for the positron experiment because of the poor amount of data. Therefore, the uncertainties and errors are also given by the full width at half maximum of an assumed Gaussian distribution centred around the obtained value. A detailed consideration of the resolution for our reaction microscope is made in Senftleben 2009. In there, the error calculation for the momenta is derived that could be adapted to our case but is omitted here.

Hence, the FWHM resolution delivers following errors:

- energy sum (see figure 4.12): $\delta E_{sum} = 12.7\text{eV}$
- positron: $\delta p^x_{\text{e}^+} = 0.39\,\text{a.u.}$, $\delta p^y_{\text{e}^+} = 0.41\,\text{a.u.}$
- electron: $\delta p^x_{\text{e}^-} = 0.54\,\text{a.u.}$, $\delta p^y_{\text{e}^-} = 0.52\text{a.u.}$
- ion: $\delta p^x_{\text{ion}} = 0.36\,\text{a.u.}$, $\delta p^y_{\text{ion}} = 1.16\text{a.u.}$

The obtained results in this work are reconstructed with an *effective* acceleration length of $l_{a+,eff} = 81.65\,\text{mm}$ and $l_{a-,eff} = 116.41\,\text{mm}$ and the drift lengths of $l_{d+,eff} = 178.40\,\text{mm}$ and $l_{d-,eff} = 247.31\,\text{mm}$ for the assumptions explained above.

5 Results

In the course of this work a kinematically complete measurement on positron impact ionization of helium by an projectile energy of 80 eV was performed during 14 days of beamtime at the NEPOMUC facility. It was possible to demonstrate that triple-coincident measurements of the scattered positron and the atomic fragments, one electron and the ion, are feasible. Despite an unexpected low positron beam current in the target and bad beam quality due to its large diameter in total about 700 events were obtained where we could reconstruct the momentum vectors of all particles in the final state. As result a number of partially integrated cross sections can be presented and we are able to discuss some aspects of the observed ionization process.

5.1 Projectile beam properties

As already mentioned in the section of the positron source (section 3.1), the NEPOMUC facility delivers a positron beam with a flux of about $10^{7}\,\mathrm{e^{+}/s}$ to the open beam port where our reaction microscope was connected to the positron beamline. After the increase of the beam size by a factor $\sqrt{10}$ caused by the adiabatic field change in the transition region (see section 3.2.4), we expected a positron current of about $10^{6}\,e^{+}/\mathrm{s}$ within a beam size of 2 mm at the reaction point since we cut out a part of the beam using an aperture. Assuming a detection efficiency of 50% for each final state particle, a count rate of about 1 Hz was calculated. However, we gained about one count in four minutes observing the peak which indicates triple coincident events in the time difference spectra. Therefore, with an estimated target density of $10^{12}\,\mathrm{cm^{-3}}$, a diameter of 2 mm for the target jet and a cross section of $\sigma_{ion} \approx 4 \times 10^{-17}\,\mathrm{cm^{2}}$ for direct ionisation for helium, a flux of less than $\sim 3 \times 10^{4}$ positrons per second crossing the target jet is obtained. For the full beam diameter which is larger than 5 mm, 10^{5} positrons per second finally reach the spectrometer (see figure 5.1). This is more than a factor of 20 less than expected and, therefore, the amount of data collected is not sufficient to obtain statistical meaningful fully differential cross sections since these require about 5×10^{5} triple coincident events. Furthermore, the large extension of the positron beam crossing the target leads to worse momentum resolution, mainly in y-direction along the jet axis..

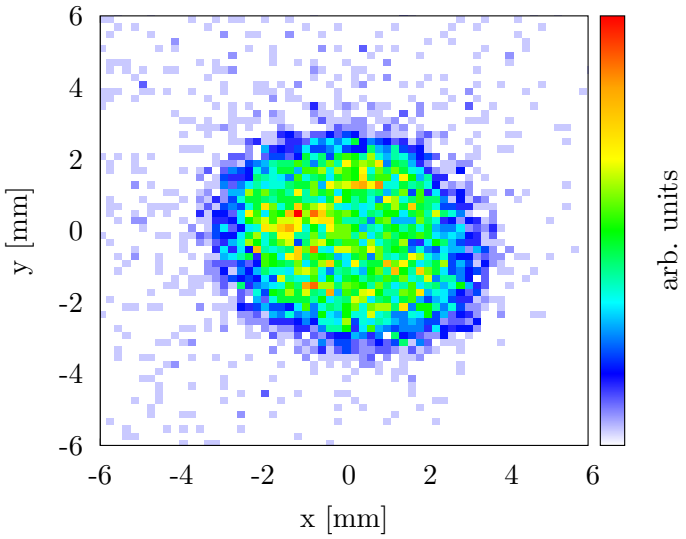

Figure 5.1: Positron beam imaged on the hexion detector.

5.2 Reconstructed momenta

As already mentioned, using a continuous beam, we are missing some momentum calibration means. For example, in the wiggle spectra of a measurement with a pulsed projectile beam, where the particle's radial position on the detector is plotted against its time-of-flight (compare figure 4.8), the time origin of the reaction and the strength of the magnetic field are accessible directly and can be determinated with a high precision[1], e.g. one gets a time resolution of about 0.1 ns. However, in our case we had to adjust the momenta of the fragments using the acceleration and drift length for both sides of the spectrometer as calibration parameter representing effective quantities. We calibrated the measurement in a way that the energy sum of the particles in the final state is centred around the energy $E_{sum} = E_{projectile} - V_{ionisation}$ where $E_{projectile}$ is the initial energy of the projectile and $V_{ionisation}$ is the ionisation potential for single ionisation of helium (compare figure 4.12). Furthermore, we used the fact that the fastest, scattered projectiles involved in an ionising reaction lose essentially only the energy necessary to ionise the helium atom. Hence, for a initial projectile energy of $E_{projectile} = 80\,\text{eV}$, we expect the distribution of the positrons' longitudinal momentum to drop down significantly at about 2.0 a.u. which corresponds to an energy of $E = 55.4\,\text{eV}$. This assumption seems to be justifiable comparing similar electron collision reactions (e.g. figure 5.3) where the fastest projectiles have an energy loss equal to the ionisation potential. In order to reduce background and false events, for further analysis only data within

[1]This calibration procedure is described in Dürr 2006

a certain range of sum energies were selected. For the following momentum spectra events with an energy sum larger than 40 eV and lower than 70 eV are taken into account.

5.2.1 Longitudinal momenta

In figure 5.2 the longitudinal momentum of each particle in the final state is plotted for the positron scattering experiment performed at NEPOMUC. The positron's momentum distribution shows a steep increase whereas its energy loss is given by the ionisation potential - this assumption was made for calibration reasons - and it reaches the maximum at 1.6 a.u.. The ejected electron has a momentum in forward direction beginning slightly below zero momentum, reaching the maximum at 0.8 a.u. and afterwards decreasing until 1.7 a.u. The two minima at 0.45 a.u and 1.15 a.u are caused by the hole in the electron detector since electrons with this certain longitudinal velocity are forced back onto the spectrometer axis by the magnetic field at the moment reaching the detector and, thus, entering the detector's hole. These minima match with the calculated values for the acceptance of the spectrometer (compare figure 4.11(b)). The gaps could be filled using further measurements with different spectrometer voltage and then a smoother momentum distribution would be obtained. It seems that the electron emerging from the atom is attracted by the positron, leaving the bound system preferentially in direction of the positively charged projectile. As can be seen in figure 5.3, for electron impact the ionised electron's longitudinal momenta are mostly centred around zero momentum. Here, the ejected electron is repelled by the equally charged projectile and attracted by the residual ion leading to post collision interaction (PCI). The longitudinal momentum distribution for the ions behaves in a reversed way. For positron impact it is centred around zero momentum while for electron impact it is shifted forward. This situation can also be seen when we look at theoretically calculated cross sections, e.g as shown in figure 5.4(a) where triple differential cross sections for electron and positron impact are presented. The 3 Coulomb (3C) wave calculation implemented by Bennaceur Najjari takes into account all mutual interactions of the three final state continuum particles and, therefore, demonstrates the expected differences in the angular distribution of the emitted electron for electron and positron impact. One can see for this specific geometry that in the case of positron scattering the electron is predominantly ejected in forward direction. The recoil peak around 180° is strongly suppressed and also shifted in forward direction whereas in the case of electron scattering this recoil peak points almost in backward direction.

The mutual dependence of the particles' longitudinal momenta for positron impact are given in figure 5.5 whereas the plot of $p^z_{e^+}$ vs. p^z_{ion} is not included since no significant correlation for this combination is found. The electron's longitudinal momentum shows a dependence on the ion's momentum in z-direction and also on the one for the positron. If the electron is ejected in forward direction, the ion

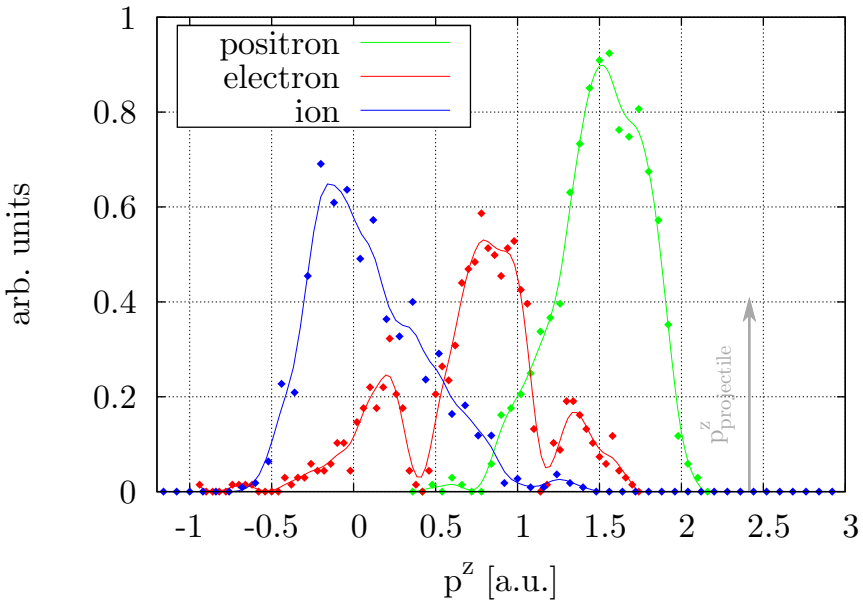

Figure 5.2: Longitudinal momentum of the scattered positron (green), the ejected electron (red) and the ion (blue). The arrow indicated in grey gives the initial momentum of the projectile.

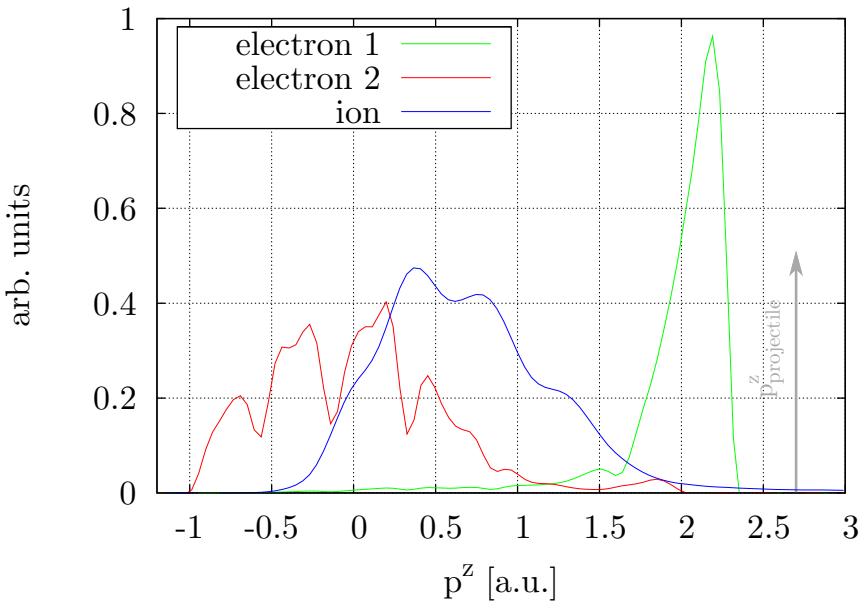

Figure 5.3: Experimentally obtained longitudinal momentum distribution for electron impact ionisation of helium with an impact energy of $E_{\text{projectile}} = 100\,\text{eV}$.

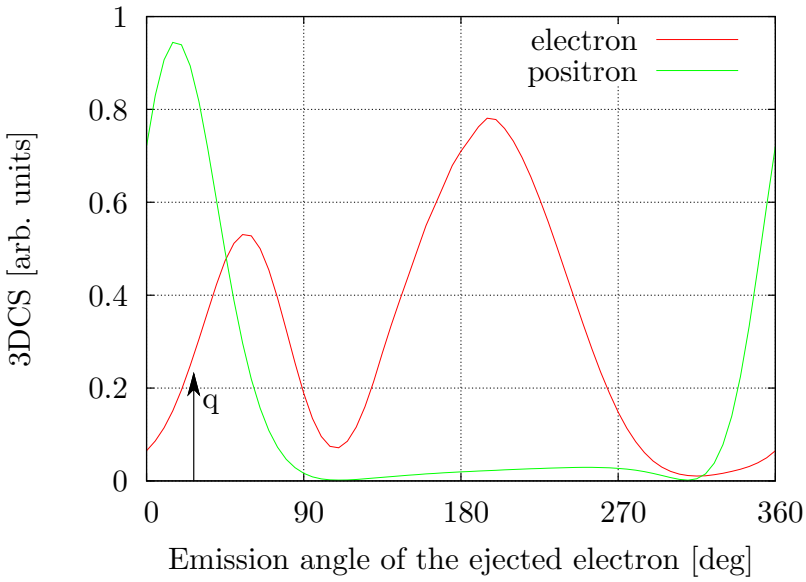

Figure 5.4: Theoretical calculation for electron and positron collision ionisation of helium in the scattering plane for a projectile scattering angle of $\theta_{\text{projectile}} = 10°$, an impact energy of $E_{\text{projectile}} = 80\,\text{eV}$ and an energy of $E_{e^-} = 10\,\text{eV}$ for the ejected electron. The triple differential cross section is plotted against the emission angle of the ejected electron. The angle of the momentum transfer q is fixed at 27°. The geometry of the ionising collision is illustrated in figure 2.2.

compensates this while carrying momentum in backward direction. This momentum balancing is characteristic for collisions with small momentum transfer to the target where the momentum sum of the target fragments is small. The correlation between positron and electron momentum can be understood by their stronger attraction if they have similar velocities and also from the fact that for higher ejected electron energy the energy loss of the scattered projectile is also higher. Furthermore, figure 5.6 shows that the energy sum within the energy resolution is independent of the longitudinal momentum of the scattered projectile and the ejected electron which indicates a proper calibration. The distribution is clustered essentially along the energy sum $E_{sum} \approx 55\,\text{eV}$ which represents single ionisation of helium for our case with an impact energy of $E_{\text{projectile}} = 80\,\text{eV}$.

5.2.2 Transverse momenta

In transversal direction, especially in y-direction, the momentum resolution is not optimal caused by the large positron beam diameter of about 5 mm in the reaction point. While in x-direction the size of the interaction volume is limited to 2 mm due

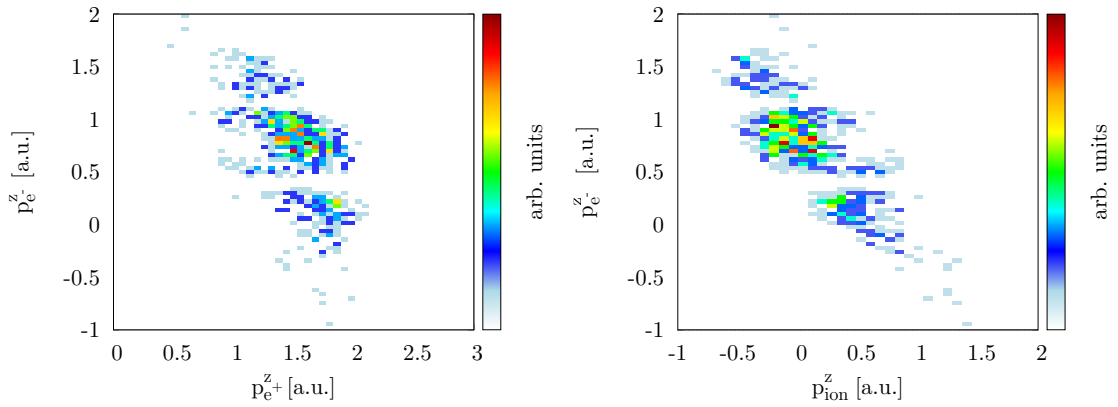

Figure 5.5: Longitudinal momentum of the electron (a) against the positron's longitudinal momentum, (b) against the longitudinal momentum of the ion.

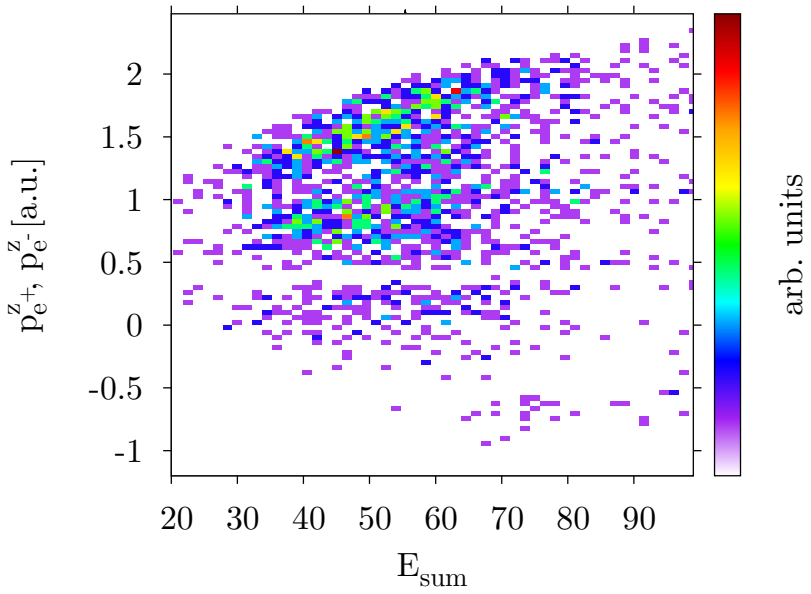

Figure 5.6: Energy sum as function of the individual longitudinal momenta of the scattered positron and the ejected electron.

to the width of the target gas jet, this is not the case in y-direction along the jet axis. The sum of the momenta of the transverse components (compare figure 5.8) are centred around zero since the momenta in x-direction and y-direction should be balanced due to momentum conservation. The distribution of the positron's transverse momentum (figure 5.8(a)) indicates that the positrons mostly are marginally deflected after the reaction and located generally around the empty origin representing the detector's hole. The electrons are also centred around the hole. Regarding figure 5.9, where the momentum in x-direction of the positron is plotted against the x-momentum of the other particle, one can identify that the positron and the ion repel each other resulting in a back-to-back motion (see figure 5.9(b)), whereas the electron's momentum in x-direction does not show a clear correlation with the respective positron momentum.

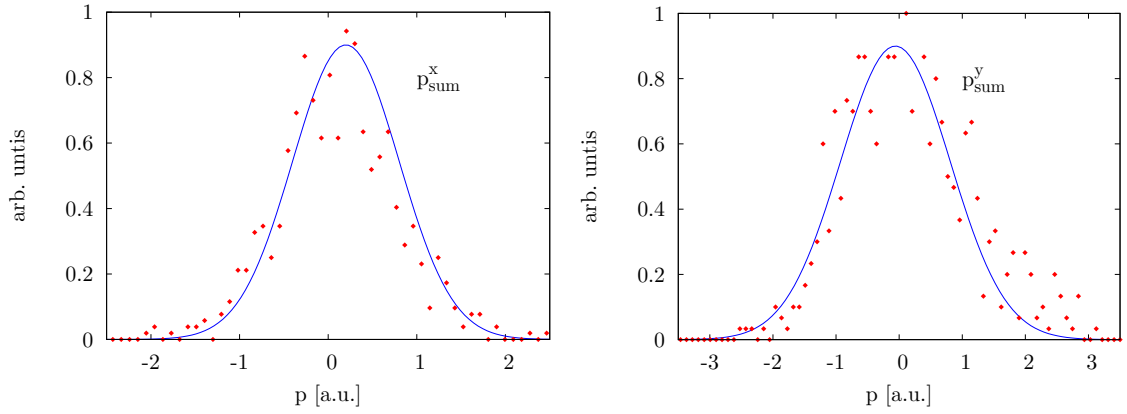

Figure 5.7: Momentum sum (a) in x-direction, (b) in y-direction.

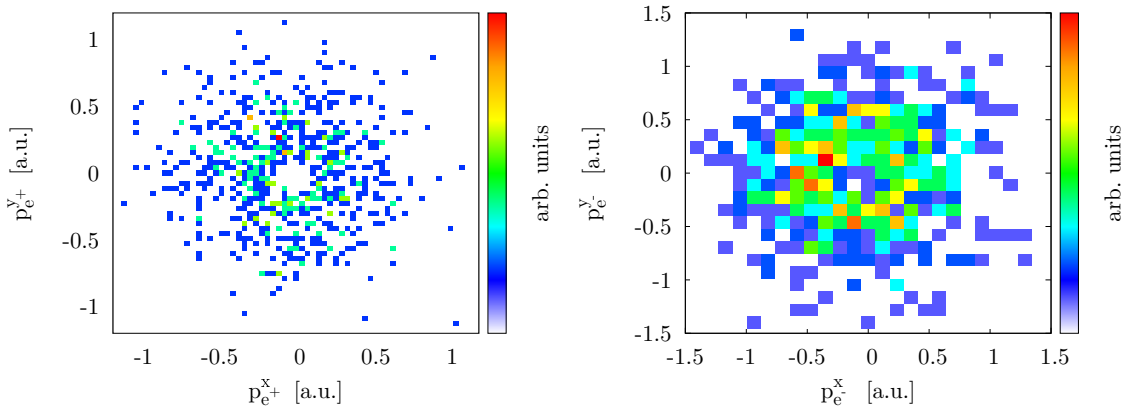

Figure 5.8: Transverse momentum (a) of the positron, (b) of the electron.

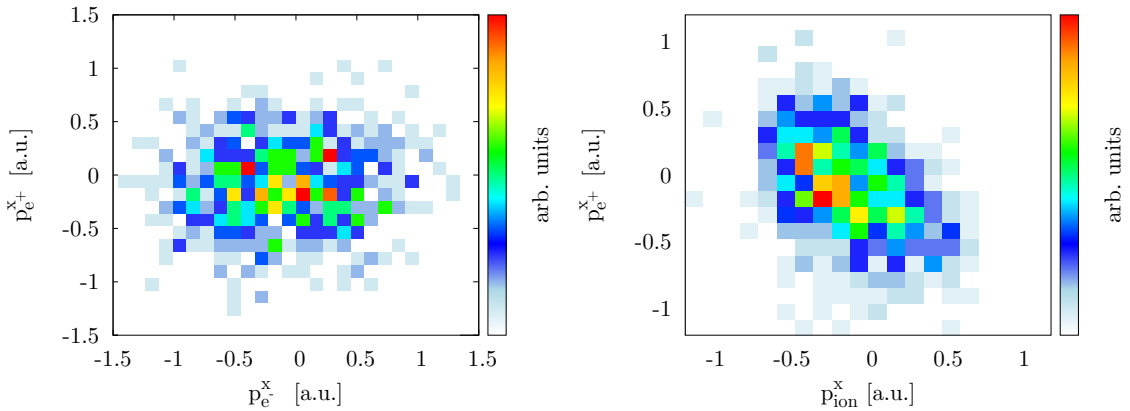

Figure 5.9: Momentum of the positron in x-direction (a) against the electron's momentum, (b) against the ion's momentum in x-direction.

6 Conclusion and outlook

The main goal of this work was to investigate the complete kinematics of positron impact ionisation of helium in order to gain information about the dynamics of this reaction. Therefore, a pilot experiment was performed which combines the technique of a reaction microscope and a low energy positron beam with a relatively high intensity provided by the NEPOMUC facility. Using this unique set-up, fully differential cross sections for the ionisation process can be obtained.

A reaction microscope originally dedicated for electron collision measurements was used to gain the three-dimensional momentum vectors of the three final state particles, which are the scattered positron, the ejected electron and the ion. The imaging technique of the reaction microscope allows to detect all charged fragments of the ionisation process in coincidence within a large range for the energy and the solid angle. With this purpose-built apparatus, low energy scattering studies in the range below 100 eV can be realised and thus, the regime, where the incoming and outgoing projectile cannot be longer regarded as small perturbation, can be accessed experimentally. Thus, this experiment was proposed to deliver data within a domain where improved theoretical calculations become available in the recent years. The experimental procedure was quite challenging since the positron beam coming from an external source had to be guided into the reaction zone within the spectrometer. This was achieved using an adiabatic decreasing magnetic field for the transition area where the reaction microscope was connected to the beamline. Furthermore, a method was developed to reconstruct the time origin of the reaction as an absolute time is not accessible for the continuous projectile beam. In a benchmark test with data obtained by a measurement with pulser signal which have been analysed on one hand using a common analysing approach and on the other hand with the algorithm resulting from this work, we showed that this method delivers correct results. Due to difficulties in the alignment of the positron beam, high background signals and a suboptimal working electron detector, less data events than expected were accumulated within the beam time. Therefore, it was not yet possible to present fully differential but only partially integrated cross sections.

However, during this work, we could demonstrate that experiments studying positron impact ionisation using a reaction microscope are feasible and deliver reasonable results. Hence, we were able to identify triple coincident events originating from the ionisation process. For these data sets, the reconstruction of momenta of the particles in the final state was possible and the momentum spectra in transverse and longitudinal direction were presented (chapter 5). For the calibration of the

measured data, some assumption had to be made due to undetermined calibration parameters. Nevertheless, qualitative conclusions, especially in comparison to electron collision studies, can be delivered. The main difference seems to affect the ejected electron which, in the case of positron scattering, emerges predominantly in forward direction contrary to electron scattering. This effect can be understood by the the opposite charge of the projectiles.

Within this work the feasibility of positron collision experiments in principle using the unique technique of a reaction microscope and a continuous beam of low energy positrons has been depicted. With the obtained experience of this pilot trial as basis for future experiments, it should be possible to acquire enough triple coincident events during a further beam time in order to extend the existing experimentally gained data in positron ionisation physics. Since in this field, so far, mainly integrated cross section or only fully differential cross section for distinguished collision geometries are available, the demand for differential cross section is undiminished. Therefore, the yield of events suitable for further analysis has to be enhanced in future experiments. This should be achievable through various approaches. The improvement of the transition between the beamline and the entrance of the reaction microscope, resulting in a less broadened beam, leads on one hand to higher count rate as the positron flux within the spectrometer is increased and on the other hand to a better momentum resolution, especially in direction of the target jet. At the moment, an adiabatic change of the magnetic field is used to guide the positron from the high magnetic field of the beam line in the lower field necessary for measurements with a reaction microscope. This solution has to be investigated in order to check why the obtained characteristics of positron beam at the reaction point was not as expected. For example, tests with an electron beam which is easier accessible than a positron beam could be performed in order to trace the beam properties with the solenoid coils producing the magnetic field. Another field open for necessary improvements is the calibration of the measurement since it turns out during this work that a proper calibration is indispensable for the following data analysis. Using a continuous projectile beam, we lose fundamental calibration factors compared to a, e.g. pulsed beam. Therefore, adjustment measurements have to be performed for the future set-up with the goal to determine the parameter given by the spectrometer's geometry which, then, could be reapplied for the analysis of the positron experiment. The yield of relevant events could further be extended by the use of other target species, for example, other noble gases like neon or argon which has an almost ten times higher cross section for direct single ionisation than helium allowing an accordingly higher coincidence count rate. The electron detector features also an area for further enhancements since the one implemented during the beam time was not well-engineered for the detection electrons. In order to obtain a complete data set about the ionisation process induced by positron impact several measurement runs with different spectrometer voltages have to be combined. This procedure allows to fill the visible blanks in momentum space caused by the specific

trajectory of the lighter particles in the magnetic field and the hole of the detectors.

Taking into account a significant improvement of future experiments through these investigations and modifications and also the knowledge gained about the topic during this work, it should be feasible to obtain fully differential cross sections for positron impact ionisation in a following measurement.

A Appendix

A.1 Applied fields and settings

In order to adjust our reaction microscope in a way that the projectile beam passes the holes in both detectors and, additionally, crosses the spectrometer axis and the target jet in the reaction point, the fields and the geometry of the spectrometer have to be adapted. Some calculated values which fit these conditions are given in table A.1. The grey shaded row represents the values that have been set during the beam time at the NEPOMUC facility. U_- represents the potential difference in $-z$-direction and U_+ in z-direction. The acceleration length l_{a-} is adjusted in $-z$-direction whereas the drift length d_{a-} is determined by double the length of l_{a-}. The acceleration and drift length in forward direction are kept at $l_{a+} = 110\,\text{mm}$ and $d_{a+} = 220\,\text{mm}$ (compare figure 3.4). E_i denotes the energy of the projectile beam when it enters the spectrometer through the hole in the electron detector.

B [Gauss]	E_i [eV]	U_- [V]	l_{a-} [mm]	t_- [ns]	U_+ [V]
7.60	55	35	61.42	47.00	62.68
7.54	70	30	70.46	47.38	46.83
7.31	60	30	67.10	48.87	49.18
7.10	80	20	80.53	50.30	27.35
6.91	40	30	57.30	51.70	46.83
6.77	80	15	84.58	52.80	19.51
6.74	90	10	90.26	53.04	12.19
6.62	74	15	83.72	54.00	19.71
6.54	60	20	75.47	54.63	29.15
6.43	80	10	89.17	55.59	12.33
6.31	65	15	81.67	56.63	20
6.15	60	15	80.43	58.07	20.51
6.10	70	10	87.81	58.54	12.53
6.00	55	15	79.02	59.63	20.88

Figure A.1: Calculated values for different spectrometer geometries and applied fields.

A.2 Implementation of the method

The method of reconstructing the time origin for a continuous beam is implemented in C++ and the actual code is shown in listing A.1. At the beginning, the threshold value `n_delta`, the start value for the positron's time-of-flight `n_to` and the initial projectile momentum `n_po` are set. Then, the first iteration step is performed by the assignment of the particles time-of-flight where `d_tpe` and `d_pr` are the differences obtained in the experiment. Using these initial times, the momenta of the particles are calculated for a first time. After initial allocation, the further iteration steps are preformed until either the control variable `nt_i` reaches the limit to the number of iteration or thevalue of the function is within a predefined interval.

```
1  /* threshold value */
2  n_delta = fParaNewtIter->NewtonDelta;
3  /* set positron's time-of-flight to start value */
4  n_to = fParaNewtIter->NewtonTo;
5  /* value for the initial momentum of the projectile */
6  n_po = fParaNewtIter->NewtonPoSum;
7
8  /* initial settings */
9  mTofPos[0] = n_to;
10 mTofElec[0] = n_to + d_tpe;
11 mTofIon[0] = n_to + d_tpr;
12 /* positron momentum */
13 fMomPos->SetInput(mTofPos, mPosPos);
14 fMomPos->CalculateMomentum();
15 mMomPos = fMomPos->GetMomentum();
16 /* electron momentum */
17 fMomElec->SetInput(mTofElec, mPosElec);
18 fMomElec->CalculateMomentum();
19 mMomElec = fMomElec->GetMomentum();
20 /* ion momentum */
21 fMomIon->SetInput(mTofIon, mPosIon);
22 fMomIon->CalculateMomentum();
23 mMomIon = fMomIon->GetMomentum();
24 /* initial projectile momentum minus momentum sum */
25 n_pzsum = n_po - (mMomElec[0]->Z() + mMomPos[0]->Z() + mMomIon
      [0]->Z());
26 nt_i = 0; // control variable
27
28 while((nt_i < fParaNewtIter->NewtonItNum) && (n_delta < fabs(
      n_pzsum)))
29 {
30   /* derivative of the momentum sum) */
```

```
31    n_dpzdsum = - (( sqrt(n_twomqu_e) * (-pelong_thelp*B_e/(
         mTofElec[0]*mTofElec[0]) + C_e/pelong_thelp +
32  D_e/pelong_thelp*cos(mTofElec[0]/pelong_thelp)) ) + ( sqrt(
       n_twomqu_p) * (-pplong_thelp*B_p/(mTofPos[0]*mTofPos[0]) +
33  C_p/pplong_thelp + D_p/pplong_thelp*cos(mTofPos[0]/
       pplong_thelp)) ) + ( prlong_const ) );
34    n_to = n_to - n_pzsum/n_dpzdsum; // iteration step of Newton
         's Method
35    nt_i ++;
36    mTofPos[0] = n_to;
37    mTofElec[0] = n_to + d_tpe;
38    mTofIon[0] = n_to + d_tpr;
39    /* positron momentum */
40    fMomPos->SetInput(mTofPos, mPosPos);
41    fMomPos->CalculateMomentum();
42    mMomPos = fMomPos->GetMomentum();
43    /* electron momentum */
44    fMomElec->SetInput(mTofElec, mPosElec);
45    fMomElec->CalculateMomentum();
46    mMomElec = fMomElec->GetMomentum();
47    /* ion momentum */
48    fMomIon->SetInput(mTofIon, mPosIon);
49    fMomIon->CalculateMomentum();
50    mMomIon = fMomIon->GetMomentum();
51    /* initial projectile momentum minus momentum sum */
52    n_pzsum = n_po - (mMomElec[0]->Z() + mMomPos[0]->Z() +
         mMomIon[0]->Z());
53  }
```

Listing A.1: Reconstruction of the reaction's time origin.

A.3 Atomic units

In atomic and molecular physics, it is convenient to use the atomic unit system which is oriented on the scale given by the hydrogen atom and the bound electron. The typical atomic dimensions are set to unity, namely the elementary charge e, the electron's rest mass m_e, the classical Bohr radius a_0, the reduced Planck constant $\hbar$ and the Coulomb constant $1/(4\pi\epsilon_0)$. Table A.3 lists some of the factors for the conversion from SI-units to atomic units (a.u.). Therein, α is the finestructure constant and c denotes the vacuum speed of light.

Quantity	Expression	Value in SI units
mass	m_e	$9.1094 \times 10^{-31}\,\mathrm{kg}$
charge	e	$1.6022 \times 10^{-19}\,\mathrm{C}$
length	a_0	$5.2918 \times 10^{-11}\,\mathrm{m}$
angular momentum	$\hbar = {}^{h}/_{2\pi}$	$1.055 \times 10^{-34}\,{}^{\mathrm{kg\,m^2}}/_{\mathrm{s}}$
energy	${}^{\hbar^2}/_{m_e a_0^2}$	$4.3597 \times 10^{-18}\,\mathrm{J}$
time	${}^{m_e a_0^2}/_{\hbar}$	$2.4189 \times 10^{-17}\,\mathrm{s}$
velocity	${}^{\hbar}/_{m_e a_0} = c \cdot \alpha$	$2.1877 \times 10^{6}\,{}^{\mathrm{m}}/_{\mathrm{s}}$
momentum	${}^{\hbar}/_{a_0}$	$1.9929 \times 10^{-24}\,{}^{\mathrm{kg\,m}}/_{\mathrm{s}}$

Figure A.2: Atomic units for selected quantities.

Bibliography

Adamczewski, J., M. Al-Turany, D. Bertini, H. G. Essel, N. Kurz, S. Linev, and M. Richter (2004). "Go4 On-Line Monitoring". In: *IEEE Transactions on Nuclear Science* 51 (June 2004), pp. 565–570. DOI: 10.1109/TNS.2004.828632.

Amoretti, M, C Amsler, G Bonomi, A Bouchta, P Bowe, C Carraro, C. Cesar, M Charlton, M. Collier, M Doser, V Filippini, K. Fine, A Fontana, M. Fujiwara, R Funakoshi, P Genova, J. Hangst, R. Hayano, M. Holzscheiter, L. Jorgensen, V Lagomarsino, R Landua, D Lindelof, E. Rizzini, M Macri, N Madsen, G Manuzio, M Marchesotti, P Montagna, H Pruys, C Regenfus, P Riedler, J Rochet, A Rotondi, G Rouleau, G Testera, A Variola, T. Watson, and D. van der Werf (2002). "Production and detection of cold antihydrogen atoms". In: *Nature* 419.6906, pp. 456–459.

Anderson, C. D. (1933). "The Positive Electron". In: *Phys. Rev.* 43.6, pp. 491–494. DOI: 10.1103/PhysRev.43.491.

Bartlett, P. L., A. T. Stelbovics, T. N. Rescigno, and C. W. McCurdy (2007). "Electron- and positron-impact atomic scattering calculations using propagating exterior complex scaling". In: *Journal of Physics: Conference Series* 88, 012011 (7pp). URL: http://stacks.iop.org/1742-6596/88/012011.

Beamson, G, H. Q. Porter, and D. W. Turner (1980). "The Collimating and Magnifying Properties of a Superconducting Field Photoelectron Spectrometer". In: *Journal of Physics E: Scientific Instruments* 13.1, pp. 64–66. URL: http://stacks.iop.org/0022-3735/13/64.

Bransden, B. H. and B. H. Joachain (2003). *Physics of Atoms and Molecules*. Ed. by B. H. Bransden. 2nd. Benjamin Cummings, p. 1112.

Bray, I. and A. T. Stelbovics (1992). "Convergent close-coupling calculations of electron-hydrogen scattering". In: *Phys. Rev. A* 46.11, pp. 6995–7011. DOI: 10.1103/PhysRevA.46.6995.

— (1993). "Convergent close-coupling calculations of low-energy positron–atomic-hydrogen scattering". In: *Phys. Rev. A* 48.6, pp. 4787–4789. DOI: 10.1103/PhysRevA.48.4787.

Brun, R. and F. Rademakers (1997). "ROOT – An object oriented data analysis framework". In: *Nuclear Instruments and Methods in Physics Research Section*

A: Accelerators, Spectrometers, Detectors and Associated Equipment 389.1-2. New Computing Techniques in Physics Research V, pp. 81 –86. ISSN: 0168-9002. DOI: DOI:10.1016/S0168-9002(97)00048-X.

Charlton, M, L. H. Andersen, L Brun-Nielsen, B. I. Deutch, P Hvelplund, F. M. Jacobsen, H Knudsen, G Laricchia, M. R. Poulsen, and J. O. Pedersen (1988). "Positron and electron impact double ionisation of helium". In: *Journal of Physics B: Atomic, Molecular and Optical Physics* 21.17, pp. L545–L549. URL: http://stacks.iop.org/0953-4075/21/L545.

Coleman, P. (2000). *Positron beams and their applications*. Ed. by P. Coleman. World Scientific Publishing Co. Pte. Ltd., p. 322.

Costello, D., D. E. Groce, D. F. Herring, and J. W. McGowan (1972). "Total scattering (Positron - Helium)". In: *Rev. Mod. Phys.* 60.3, pp. 701–779. DOI: 10.1103/RevModPhys.60.701.

Dirac, P. A. M. (1928). "The Quantum Theory of the Electron". In: *Proceedings of the Royal Society of London. Series A* 117.778, pp. 610–624. DOI: 10.1098/rspa.1928.0023. eprint: http://rspa.royalsocietypublishing.org/content/117/778/610.full.pdf+html.

Dorn, A., R. Moshammer, C. D. Schröter, T. J. M. Zouros, W. Schmitt, H. Kollmus, R. Mann, and J. Ullrich (1999). "Double Ionization of Helium by Fast Electron Impact". In: *Phys. Rev. Lett.* 82.12, pp. 2496–2499. DOI: 10.1103/PhysRevLett.82.2496.

Dürr, M, C Dimopoulou, A Dorn, B Najjari, I Bray, D. V. Fursa, Z. Chen, D. H. Madison, K Bartschat, and J Ullrich (2006). "Single ionization of helium by 102 eV electron impact: three-dimensional images for electron emission". In: *Journal of Physics B: Atomic, Molecular and Optical Physics* 39.20, pp. 4097–4111. DOI: 10.1088/0953-4075/39/20/008. URL: http://stacks.iop.org/0953-4075/39/4097.

Dürr, M. (2006). "Electron Induced Break-up of Helium: Benchmark Experiments on a Dynamical Four-Body Coulomb System". PhD thesis. Ruperto-Carola University of Heidelberg.

Ehrhardt, H., M. Schulz, T. Tekaat, and K. Willmann (1969). "Ionization of Helium: Angular Correlation of the Scattered and Ejected Electrons". In: *Phys. Rev. Lett.* 22.3, pp. 89–92. DOI: 10.1103/PhysRevLett.22.89.

Ferger, T. (2006). "Untersuchung der Mehr-Teilchen-Dynamik in Stössen von 200 keV H^- mit Helium und Aufbau eines kalten atomaren Wasserstofftargets für Ionisationsexperimente". Diss. Ruprecht-Karls-Universität Heidelberg.

Fischer, D. (2000). "Aufbau eines Reaktionsmikroskops zur Untersuchung von Ion-Atom-Stoe/ssen". Diplomarb. Fakultät für Physik - Albert-Ludwigs-Universität Freiburg im Breisgau.

Fursa, D. V. and I. Bray (1995). "Calculation of electron-helium scattering". In: *Phys. Rev. A* 52.2, pp. 1279–1297. DOI: 10.1103/PhysRevA.52.1279.

Gabrielse, G, N. Bowden, P Oxley, A Speck, C. Storry, J. Tan, M Wessels, D Grzonka, W Oelert, G Schepers, T Sefzick, J Walz, H Pittner, T. Hansch, E. Hessels, and ATRAP Collaboration (2002). "Driven production of cold antihydrogen and the first measured distribution of antihydrogen states". English. In: *Physical Review Letters* 89.23. DOI: 10.1103/PhysRevLett.89.233401.

Gilbert, S. J., C. Kurz, R. G. Greaves, and C. M. Surko (1997). "Creation of a monoenergetic pulsed positron beam". In: *Applied Physics Letters* 70.15, pp. 1944–1946. DOI: 10.1063/1.118787. URL: http://link.aip.org/link/?APL/70/1944/1.

Haag, N. (2006). "Kinematisch vollständige Experimente zur elektronenstoßinduzierten Ionisation und Dissoziation von H2-Molekülen". Diplomarb. Max-Planck Institute of Nuclear Physics.

Höhr, C. (2004). "Kinematisch vollständige Experimente zur Ionisation im Elektronenstoß und Laserfeld". Diss. Ruprecht-Karls-Universität Heidelberg.

Hsu, T. and J. L. Hirshfield (1976). "Electrostatic energy analyzer using a nonuniform axial magnetic field". In: *Review of Scientific Instruments* 47.2, pp. 236–238. DOI: 10.1063/1.1134594. URL: http://link.aip.org/link/?RSI/47/236/1.

Hugenschmidt, C., G. Kögel, R. Repper, K. Schreckenbach, P. Sperr, B. Straßer, and W. Triftshäuser (2002). "Monoenergetic positron beam at the reactor based positron source at FRM-II". In: *Nuclear Instruments and Methods in Physics Research Section B: Beam Interactions with Materials and Atoms* 192.1-2, pp. 97 –101. ISSN: 0168-583X. DOI: 10.1016/S0168-583X(02)00788-7.

Hugenschmidt, C., B. Löwe, J. Mayer, C. Piochacz, P. Pikart, R. Repper, M. Stadlbauer, and K. Schreckenbach (2008). "Unprecedented intensity of a low-energy positron beam". In: *Nuclear Instruments and Methods in Physics Research Section A: Accelerators, Spectrometers, Detectors and Associated Equipment* 593.3, pp. 616 –618. ISSN: 0168-9002. DOI: DOI:10.1016/j.nima.2008.05.038.

Jackson, J. D. (1975). *Classical Electrodynamics*. 2nd. Wiley & Sons (New York).

Janert, P. K. (2007). *Gnuplot in Action: Understanding Data with Graphs*. Ed. by P. K. Janert. 1st. Manning Pub, p. 396.

Kauppila, W. E. and T. S. Stein (1989). "Comparisons of Positron And Electron Scattering By Gases". In: *Advances In Atomic, Molecular, and Optical Physics*. Ed. by S. D. Bates and B. Bederson. Vol. 26. Advances In Atomic, Molecular, and Optical Physics. Academic Press, pp. 1 –50. DOI: DOI:10.1016/S1049-250X(08)60059-2.

Kelley, T. W. . C. (2007). *gnuplot - An Interactive Plotting Program*. http://www.gnuplot.info/. URL: http://www.gnuplot.info/.

Knudsen, H, L Brun-Nielsen, M Charlton, and M. R. Poulsen (1990). "Single ionization of H2, He, Ne and Ar by positron impact". In: *Journal of Physics B: Atomic, Molecular and Optical Physics* 23.21, pp. 3955–3976. URL: http://stacks.iop.org/0953-4075/23/3955.

Köver, A, G Laricchia, and M Charlton (1993). "Ionization by positrons and electrons of Ar at zero degrees". In: *Journal of Physics B: Atomic, Molecular and Optical Physics* 26.17, pp. L575–L580. URL: http://stacks.iop.org/0953-4075/26/L575.

Kruit, P and F. H. Read (1983). "Magnetic field paralleliser for 2 π; electron-spectrometer and electron-image magnifier". In: *Journal of Physics E: Scientific Instruments* 16.4, pp. 313–324. URL: http://stacks.iop.org/0022-3735/16/313.

Lampton, M., O. Siegmund, and R. Raffanti (1987). "Delay line anodes for microchannel-plate spectrometers". In: *Review of Scientific Instruments* 58.12, pp. 2298–2305. DOI: 10.1063/1.1139341. URL: http://link.aip.org/link/?RSI/58/2298/1.

Langbrandtner, C. (2007). "Experimente zur Ionisation von atomarem Wasserstoff im Ionenstoß". Diplomarb. Ruprecht-Karls-Universität Heidelberg.

Laricchia, G., S. Armitage, A. Köver, and D. Murtagh (2008). "Ionizing Collisions by Positrons and Positronium Impact on the Inert Atoms". In: *Advances In Atomic, Molecular, and Optical Physics*. Ed. by A. et al. Vol. 56. Advances In Atomic, Molecular, and Optical Physics. Academic Press, pp. 1 –47. DOI: DOI:10.1016/S1049-250X(08)00010-4.

Martin, C., P. Jelinsky, M. Lampton, R. F. Malina, and H. O. Anger (1981). "Wedge-and-strip anodes for centroid-finding position-sensitive photon and particle detectors". In: *Review of Scientific Instruments* 52.7, pp. 1067–1074. DOI: 10.1063/1.1136710. URL: http://link.aip.org/link/?RSI/52/1067/1.

Massey, S. (1976). "Slow positrons in gases". In: *Phys. Today* 29, pp. 42–51.

Mergel, V. (1996). "Dynamische Elektronenkorrelationen in Helium". Diss. Goethe Universität Frankfurt.

Miller, D. R. (1988). "Free jet sources". In: *Atomic beam methods*. Ed. by G. Scoles. Vol. 1. 1. Oxford University Press, pp. 13–53.

Moshammer, R., J. Ullrich, M. Unverzagt, W. Schmitt, and B. Schmidt-Böcking (1996). "A 4π recoil-ion electron momentum analyzer: A high-resolution 'microscope' for the investigation of the dynamics of atomic, molecular and nuclear reactions". In: *Nuclear Instruments and Methods in Physics Research B* 108, pp. 425–445. DOI: 10.1016/0168-583X(95)01259-1.

Pflüger, T. (2008). "Electron Impact Single Ionization of Small Argon Cluster". Diplomarb. Max-Planck Institute of Nuclear Physics.

Phillips, W. D. and H. Metcalf (1982). "Laser Deceleration of an Atomic Beam". In: *Phys. Rev. Lett.* 48.9, pp. 596–599. DOI: 10.1103/PhysRevLett.48.596.

Piochacz, C., G. Kögel, W. Egger, C. Hugenschmidt, J. Mayer, K. Schreckenbach, P. Sperr, M. Stadlbauer, and G. Dollinger (2008). "A positron remoderator for the high intensity positron source NEPOMUC". In: *Applied Surface Science* 255.1. Proceedings of the Eleventh International Workshop on Slow Positron Beam Techniques for Solids and Surfaces, pp. 98 –100. ISSN: 0169-4332. DOI: DOI:10.1016/j.apsusc.2008.05.286.

Press, W. H. (2007). *Numerical recipes: the art of scientific computing*. Ed. by 3rd. Cambridge University Press.

Ramsauer, C. (1922). "Über den Wirkungsquerschnit der Gasmoleküle gegenüber langsamen Elektronen". In: *Annalen der Physik* 371.24, S. 546–558. DOI: 10.1002/andp.19223712403. URL: http://dx.doi.org/10.1002/andp.19223712403.

Rescigno, T., M Baertschy, W. Isaacs, and C. McCurdy (1999). "Collisional breakup in a quantum system of three charged particles". In: *SCIENCE* 286.5449, pp. 2474–2479.

R.L. Wahl, J. B. (2002). *Principles and Practice of Positron Emission Tomography*. Ed. by R. Wahl. Lippincott Williams and Wilkins, p. 462.

RoentDek (2002). "3-dimensional resolving Wedge-and-Strip-Detector with image charge coupling". In: *Manual* 1, p. 19.

Ruark, A. E. (1945). "Positronium". In: *Phys. Rev.* 68.11-12, p. 278. DOI: 10.1103/PhysRev.68.278.

Rutherford, E (1911). "The Scattering of α and β Particles by Matter and the Structure of the Atom". In: *Philosophical Magazine* 21.6, p. 669.

Sakurai, J. J. (1993). *Modern Quantum Mechanics*. Ed. by A. Wesley. Addison Wesley, p. 500.

Schultz, D. R., R. E. Olson, and C. O. Reinhold (1991). "Recent advances in the comparison of matter- and antimatter-atom collisions". In: *Journal of Physics B: Atomic, Molecular and Optical Physics* 24.3, pp. 521–558. URL: http://stacks.iop.org/0953-4075/24/521.

Schultz, P. J. and K. G. Lynn (1988). "Interaction of positron beams with surfaces, thin films, and interfaces". In: *Rev. Mod. Phys.* 60.3, pp. 701–779. DOI: 10.1103/RevModPhys.60.701.

Senftleben, A. (2009). "Kinematically complete study on electron impact ionisation of aligned hydrogen molecules". PhD thesis. Combined Faculties for the Natural Sciencs and for Mathematics of the Ruperto-Carola University of Heidelberg, Germany.

Spiegelhalder, F. M. (2005). "Setting up a Lithium Magneto-Optical Trap as a Target for a Reaction Microscope". Dipl thesis. Max-Planck Institute of Nuclear Physics.

Stelbovics, A. T., I. Bray, D. V. Fursa, and K. Bartschat (2005). "Electron-impact ionization of helium for equal-energy-sharing kinematics". In: *Phys. Rev. A* 71, p. 052716. DOI: 10.1103/PhysRevA.71.052716.

Surko, C. M., M Leventhal, W. S. Crane, A Passner, F Wysocki, T. J. Murphy, J Strachan, and W. L. Rowan (1986). "Use of Positrons to Study Transport in Tokamak Plasmas". In: *Review of Scientific Instruments* 57.8, Part 2, pp. 1862–1867.

Suzuki, R., T. Ohdaira, T. Mikado, A. Uedono, H. Ohgaki, T. Yamazaki, and S. Tanigawa (1997). "Moderation of Positrons Generated by an Electron Linac". In: *Materials Science Forum* 255 - 257, pp. 114–118. DOI: 10.4028. URL: www.scientific.net/MSF.255-257.114.

Townsend, J. and V. Bailey (1922). "The motion of electrons in argon". English. In: *Philosophical Magazine* 43.255, Sp. Iss. 6th series, pp. 593–600. ISSN: 1478-6443.

Wiza, J. L. (1979). "Microchannel Plate Detectors". In: *Nucl. Instrum. Methods* 162, pp. 60–1. DOI: 10.1.1.119.933.

Wu, H., I. Bray, D. V. Fursa, and A. T. Stelbovics (2004). "Convergent close-coupling calculations of positron–helium scattering at intermediate to high energies". In: *Journal of Physics B: Atomic, Molecular and Optical Physics* 37.6, pp. 1165–1172. URL: http://stacks.iop.org/0953-4075/37/1165.

Zhou, S., H. Li, W. E. Kauppila, C. K. Kwan, and T. S. Stein (1997). "Measurements of total and positronium formation cross sections for positrons and electrons scattered by hydrogen atoms and molecules". In: *Phys. Rev. A* 55.1, pp. 361–368. DOI: 10.1103/PhysRevA.55.361.